Geophys. J. Int. (2002) **148,** 542–561

Numerical models of the evolution of accretionary wedges and fold-and-thrust belts using the distinct-element method

D. R. Burbidge* and J. Braun

Research School of Earth Sciences, Geoscience Australia, GPO Box 378, *Canberra, ACT,* 2601, *Australia. Email: david.burbidge@ga.gov.au*

Accepted 2001 August 10. Received 2001 June 13; in original form 2000 March 27

SUMMARY

A 2-D numerical model is used to investigate the evolution of accretionary wedges and fold-and-thrust belts. The numerical method is based on the distinct-element method (DEM). Unlike many continuum numerical models, DEM allows localization to occur even after substantial amounts of deformation. The method is used to study the evolution of simple accretionary wedges and thrust belts with a rigid backstop and base. Experiments are done with a large range of coefficients of interelement friction (μ_e) and element-wall friction (μ_b). Two modes of deformation, which depend mainly on μ_b, are observed. For the weak base case (low μ_b), the dominant mode is frontal accretion by 'pop-up' structures at or near the toe of the wedge. For the strong base case (high μ_b), uplift is concentrated near the back of the wedge, and is accompanied by underthrusting along a flat-ramp-flat (or 'staircase') thrust fault structure. At intermediate values of μ_b, the wedge oscillates between the two modes of deformation. During periods of frontal accretion, normal faulting sometimes occurs in regions where the material has thickened considerably. The transition between the two modes of deformation is found to be a strong function of μ_b but a weak function of μ_e. A simple explanation of the experimental results is made using the principle of work minimization. Comparisons between the results and some accretionary wedges/fold-and-thrust belts are also made.

Key words: collision belts, crustal deformation, faulting, lateral heterogeneity, normal faulting, numerical techniques.

1 INTRODUCTION

Analogue models have long been used to develop our understanding of the mechanics of upper crustal deformation (Hubbert 1937). The majority of these models use a granular material, such as sand (e.g. Burbidge & Braun 1998; Cobbold & Castro 1999 and references therein). To first order, both sand and the upper crust behave mechanically as a Coulomb material (see Lambe & Whitman 1968; Byerlee 1978). As a result, they accommodate deformation in a very similar way. Deformation in analogue models is usually localized along a limited number of structures that are similar to the faults seen in the crust. However, analogue models are often limited in the range of problems that they can examine. For example, it is often difficult to find a range of granular materials with different coefficients of internal friction.

The other method commonly used to model the upper crust is to solve the equations of force balance numerically. The vast majority of these models use the finite-element method (FEM) or similar techniques (e.g. Beaumont *et al.* 1994). These models are more flexible than analogue models because they can consider a wider range of rheologies and boundary conditions. However, the numerical methods usually have some difficulty in modelling large amounts of deformation accurately, owing to excessive mesh deformation (or interpolation) in the regions of localization. For example, they can have difficulty in modelling the succession of faults in intricate fans observed in analogue models and the upper crust. Commonly used numerical models are usually built around a continuity assumption at some scale of the model that prevents the elements from separating, e.g. continuity of displacement over element boundaries in FEM models. This makes large amounts of strain localization very difficult.

In this paper, we use a numerical method that models each element as being discrete and separable from its initial neighbours. The motivation for numerically modelling the crust in this way comes from analogue models. However, we are using the method here to understand the evolution of accretionary prisms and thin-skinned thrust belts, we are not attempting to reproduce the results of analogue models.

Our method is based on the distinct-element method (DEM) first developed by Cundall & Strack (1979) to model the deformation of discontinua. The method combines the flexibility of numerical modelling with the localization capabilities of

* 10 Piddington St. Watson, ACT 2602, Australia

analogue modelling. Most applications of the DEM method are conducted on the scale of the discontinuities of the problem [e.g. sand grains or fault blocks (Cundall & Hart 1989; Homberg *et al.* 1997)]. In our model, the elements are regarded as the lower limit of the resolution at which we wish to model the problem. The material parameters are chosen so as to reproduce the desired bulk properties. For example, the size of the elements are chosen to give the model a total initial height of 1 km [consistent with the incoming sediment thickness of most accretionary wedges, which varies between 400 m and 2 km for most systems (Lallemand *et al.* 1994)] and the elastic properties were chosen to give a bulk Young's modulus of 10 GPa [which is within the acceptable range for rocks such as sandstone (Turcotte & Schubert 1982)].

To differentiate this code from more standard DEM models, the code has been dubbed the distinct-element crustal model (DECM). While DEM models have been used to model a wide variety of discontinuous problems, to the best of the authors' knowledge, it has not been used to model geodynamic processes in this way before [i.e. where the elements of the model are considered to be just the lowest limit at which we wish to model the problem, rather than as discontinuous blocks that exist in nature (e.g. Sassi & Faure 1997)]. Others have used a distinct-element approach to model the evolution of sandbox experiments, in which each element represents an individual grain of sand (e.g. Hryciw *et al.* 1997). However, the elements in our model should be thought of as being similar to the elements of a finite-element model; they just represent a region of crustal rock. In fact, one can show that the distinct-element method can be recast into an unusual type of finite-element method (Pande *et al.* 1990). Similarly to the FEM, DEM is quite general and can handle a range of constitutive behaviour (Pande *et al.* 1990). Its main advantage over FEM approaches is its ability to handle discontinuua (such as the upper crust). The closest published work in which a DEM is used in this way is by Saltzer & Pollard (1992) who attempted to reproduce extensional sandbox experiments with a DEM. The difference here is that we are attempting to use a DEM as an alternative to a FEM to solve a mechanical problem at the scale of the crust; the suitability of the method depends on how well geologically observed structures are reproduced. The similarity of the observed structures to sandbox models is secondary. Our main purpose is to demonstrate that the distinct-element method can model a complex crustal deformation problem, such as the evolution of accretionary prisms and thrust belts.

It has been known for some time that there are two principal mechanisms for accretion in accretionary prisms: (1) frontal accretion or (2) underthrusting or back accretion (Platt 1986). Frontal accretion consists of off-scraping the incoming sediment/crustal material and incorporating it into the wedge at the front of the prism. Deformation is mostly accommodated by pro-thrusts [thrusts dipping towards the backstop (Willett *et al.* 1993)] and only marginally by retro-thrusts (thrusts dipping towards the toe). Similar behaviour has been demonstrated in numerous sandbox models (e.g. Davis *et al.* 1983). Frontal accretion has been observed in a large number of accretionary prisms/fold-and-thrust belts [e.g. the Canadian Rockies, the European Alps, the Oregon coast accretionary prism, the Nankai accretionary prism etc., see Platt (1986) and references therein]. In contrast, when the accretionary wedge accommodates the deformation by underthrusting, incoming material can be thrust underneath the wedge for tens of kilometres before being uplifted. It follows that sediments may undergo low-temperature metasomatism if they are buried sufficiently deeply. They are then uplifted near the backstop of the prism. This is one possible explanation for the presence of metasomatized sediments near the rear of some prisms (Platt 1986). Sometimes the same wedge can display the two different modes of accretion along a single subduction zone [e.g. the Alaskan accretionary wedge (Kusky *et al.* 1997; Gulick *et al.* 1998; Gutscher *et al.* 1998a)].

The two principal modes of accretion have been observed recently in sandbox models by Gutscher *et al.* (1996, 1998a,b) and have been observed separately in other analogue models (e.g. Cowan & Silling 1978; Lui *et al.* 1992). Gutscher *et al.* (1998a,b) found that deformation in accretionary wedges may oscillate between frontal accretion and underthrusting without any changes in the boundary conditions. As a result, the overall slope of the wedge changes through the experiment. In their experiments, frontal accretion was found to occur more often when the smallest of their two basal friction materials was used.

In this project we examine a range of internal and basal friction coefficients in order to quantify this effect. The range of rheologies tested would be beyond the capabilities of standard analogue models and the amount of deformation we reproduce is beyond the capabilities of most standard numerical models.

2 THE NUMERICAL METHOD

2.1 Distinct-element crustal model

In any DEM model, the material is divided into elements that in principle can be any shape or size. In DECM, the material is discretized into nodes that only interact directly with each other when they are a specific distance apart. This can be visualized as a set of 2-D circular elements that are defined to be in 'contact' when they overlap with either each other or with a wall. Since the elements are allowed to overlap, this is sometimes known as a soft-contact DEM (Cundall & Hart 1989). A circular interaction distance requires less computational effort than any other shape and this therefore allows more elements to be used for the same amount of computation time (Pande *et al.* 1990). However, the contact between the elements is modelled as if a flat plane existed between them [i.e. a linear elastic force is exerted between the elements rather than Hertzian elasticity, for example (Johnson 1985)]. This is probably reasonable for crustal rock, since the elastic response is approximately linear along joints until the yield strength is reached (Touloukian *et al.* 1989). In the code, the circular nature of the elements should be interpreted as being a 'reaction distance' between regions of crustal rock. When the centroids of elements approach each other so that the circles overlap, the regions of crustal rock they represent begin to interact along a joint that is assumed to exist between them. When they are further away they do not influence each other directly.

2.2 Interaction between the elements

If two elements are in contact, a force normal to the contact plane and proportional to the amount of overlap (F_n) repels the elements from one another (i.e. linear elasticity). A shear force proportional to the amount of displacement perpendicular to the contact (F_s) is also exerted on each element. This shear force

is limited to be less than $\mu_e F_n$, where μ_e is the coefficient of friction between the elements. Analogous reasoning is used if the element is in contact with one of the walls (with μ_e being replaced by the element to wall coefficient of friction, μ_b).

Contact damping (i.e. damping directly proportional to the relative velocity between elements in contact) is used to damp down vibrations in the model and to ensure that the kinetic energy does not become excessive [i.e. the kinetic energy must be less than 1 per cent of the average change in potential energy over the period, see Burbidge (2000) for more details]. The damping, time step and strain increment per time step ($\delta\varepsilon$) are tuned to ensure that any sudden increase in kinetic energy (e.g after a major faulting event) is quickly damped (within 1000–2000 time steps). Global damping, as proposed by Cundall & Strack (1979), was not used as this seemed to artificially inhibit large translations of the elements.

The time step (δt) is chosen to be a small fraction of the period of a 1-D simple harmonic oscillator with the same stiffness and damping as the element. This ensures that the vibrations (both translationally and rotationally) are correctly integrated (see the Appendix).

A large number of small experiments were conducted to find the 'best' values of δt, $\delta\varepsilon$ and γ_n which correctly integrate the problem, damp out the kinetic energy quickly (i.e. in a few thousand time steps), and complete the problem as quickly as possible (in real time). These integration parameters are interrelated. For example, if we damp the kinetic energy more quickly (i.e. in fewer time steps) we can increase $\delta\varepsilon$. For the experiments considered here, we settled on using integration parameters that did not change during the experiment, since this produced reasonably accurate and stable results [e.g. no 'numerical heating' effects (Allen & Tildesley 1987)]. A more detailed discussion can be found in Burbidge (2000).

Details of the parameters used in the experiments described in this paper are given in Table 1. Typical runs take 2–3 days to complete on a Sun Ultra 5 and require $1–2 \times 10^6$ time steps. Since the system is deformed very slowly, it is quasi-static and so the results are independent of the amount of deformation per time step (so long as this is kept small).

Table 1. The properties of the crust used in the models. Damping is expressed as a fraction of the critical damping for a 1-D simple harmonic oscillator (SHO) with the same mass and stiffness of the element. Similarly, the time step is expressed as the fraction of the period of a SHO.

Normal stiffness (k_n)	1×10^{10} N m^{-1}
Shear stiffness (k_s)	1×10^{10} N m^{-1}
Initial height of the pack	1 km
Number of layers in the model	15
Number of elements along the base	600
Total number of elements in the model	8993
Radius of an element	38 m
Density of the elements	2500 kg m^{-2}
Acceleration due to gravity	9.80 m s^{-2}
Contact damping (normal and shear)	0.01
Time step, δt	$0.01/2\pi$
Strain increment per time step, $\delta\varepsilon$	$1–2 \times 10^{-7}$
Total strain at the end of a run	0.5
Cohesion (interelement & element-wall)	0 N m^{-2}
μ_e	0.2–10.0
μ_b	0.2–100.0

The elements in the model are allowed to come to equilibrium from their initial locations before any run is started. Equilibrium is assumed to be reached when the maximum net force on any element is less than one hundredth of its weight (in newtons). More details of the method are given in the appendix.

2.3 Initial and boundary conditions

The boundary conditions of the experiment are made similar to typical ones used in other numerical or analogue models of accretionary prisms/thrust belts. The initially undeformed material lies on a rigid base, and is compressed by a vertical rigid backstop. The rigid base model is reasonable for small prisms (less than a few kilometres thick) which would be supported by the elastic strength of the lithosphere (Turcotte & Schubert 1982). The model is scale-independent so the experimental result would be the same if the initial height of the material was (say) 10 km instead of 1 km (and the elastic stiffness was appropriately rescaled). However, factors such as isostasy and any change in rheology with pressure would become increasingly important for larger prisms (Platt 1986). The experiments described here can be applied to these larger systems, so long as one is willing to accept the model as a first-order approximation.

The backstop in the model could represent the overriding plate, or previously accreted but lithified sediments that deform much more slowly than the incoming sedimentary material (Platt 1986). The model is run in the reference frame of the subducting plate (i.e. the right-hand wall moves to the left in Fig. 1a). A few test runs were done in the reference frame of the overriding plate (i.e. with the right-hand wall fixed and the left-hand wall and base moving from left to right). They showed no significant difference with runs preformed in the opposite reference frame.

Elements all have the same radius and are initially in a triangular lattice packed array (see Fig. 2). This makes the material weak along horizontal layers (bedding planes) and the 30° dipping lattice planes. The initial faults formed predominantly along these planes. This may be roughly considered as being analogous to pre-existing bedding planes and faults in the crust. The material is thus not isotropic but is initially uniformly anisotropic (i.e. the anisotropy is the same at different points in the model). This was done deliberately in order to investigate the effect of this initial regular anisotropy. Sedimentary packages are often layered, and this may introduce a horizontal anisotropy. It is quite different to the initial conditions used in most numerical or analogue models of accretionary prisms/thrust belts. In DECM, this anisotropy disappears once the prism deforms and the system loses its initial packing. The interelement and basal friction are held constant for each run.

2.4 Bulk friction

Simple shear box tests (see Fig. 1b) were conducted to estimate the bulk properties of the material. A diagram of the results from a shear box test is shown in Fig. 3. The bulk coefficient of friction was estimated from the shear stress and normal stress exerted along a plane through the middle of a box [this experiment is similar to shear box tests used to determine the

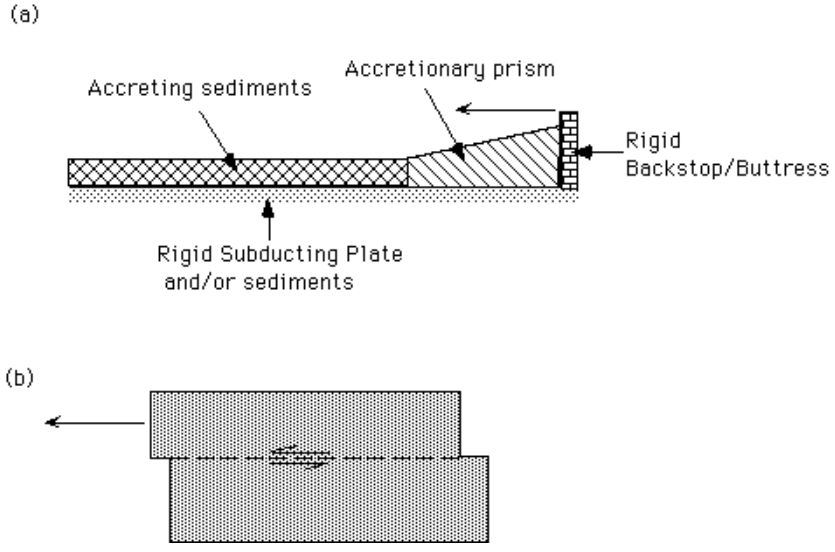

Figure 1. (a) Highly simplified schematic diagram of the model. The model is located in the reference frame of the incoming material. Hence, the rigid backstop moves, while the incoming sediment/crustal material is stationary in this reference frame. (b) Schematic plot of a standard shear box experiment.

bulk properties of granular materials (Lambe & Whitman 1968)]. A constant force is exerted on the elements in contact with the top wall. Elements can pass through the top wall. Elements were initially in a triangular lattice packing.

Broadly similar results were found to those of Oger *et al.* (1998) and Morgan (1999). As the top part of the right-hand wall is moved from right to left, the stress exerted on the model increases until eventually the experiment breaks. The stress at which this occurs is called the yielding stress. The behaviour of the system is complex and is influenced by μ_e, the packing and the amount of stress exerted on the top wall. This type of rheology is difficult to describe with a simple set of consitutive equations. Increasing μ_e increases the yielding stress but has a smaller influence on the post-yield behaviour. Higher values of μ_e mean that the system is initially 'stronger' (i.e. a higher stress is required to break it). However, increasing the stress exerted on the elements in contact with the top wall forces the material to remain in a configuration closer to its initial triangle lattice packing and also prevents faulting in the upper section of the experiment. This reduces the difference between the yield stress and the post-yield stress (Burbidge 2000).

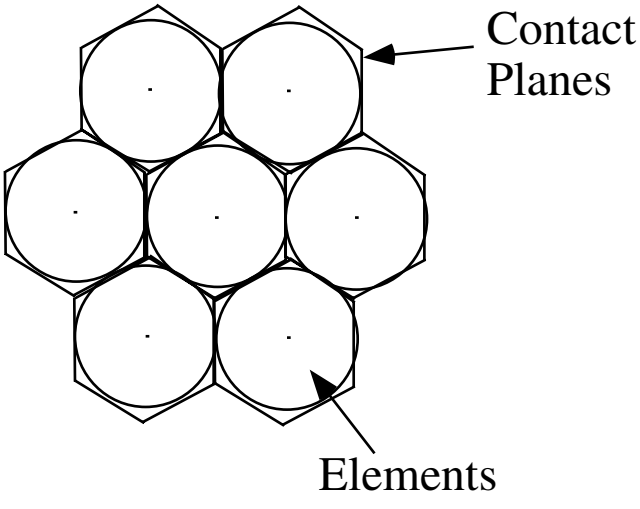

Figure 2. A magnified view of the elements in the model. All elements are circular, and are initially arranged in a triangular lattice pattern. Elements interact along the contact planes between the elements, when the elements overlap.

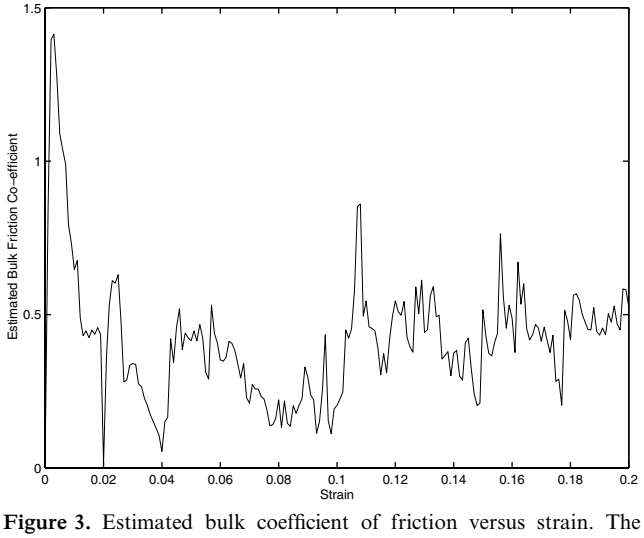

Figure 3. Estimated bulk coefficient of friction versus strain. The material is undergoing horizontal shear in a shear box experiment (Fig. 1b). Elements initially have triangle lattice packing and $\mu_e = 0.5$. The stress exerted on elements in contact with the top wall is held constant at 1 MPa. As the material is sheared, the stress exerted on the material builds up linearly until it reaches the failure stress. At failure, the bulk friction drops dramatically, as the material fails (by fracture). The precise mechanisms of this failure (i.e. the type and location of the faults) depends on the material parameters and boundary conditions (particularly the top wall stress). The material has a lower bulk friction after failure since the initial packing is broken and the material is therefore weaker.

These bulk properties are analogous to those found in the crust. The initially compacted sediment is strong and can accommodate the deformation elastically. Eventually it breaks and a fault forms, which greatly weakens the material. However, if the material is compressed sufficiently it can 'heal' back up to its original strength. The 'bumpy' nature of the fault plane also gives the model 'stick–slip' behaviour (i.e. the shape of the elements produces 'asperities' in the fault plane). Choosing a triangular lattice initial packing enhances these effects when compared with, say, a random initial packing. Since TLP is the densest possible packing, any other arrangement is less dense and thus weaker (Lambe & Whitman 1968). This makes TLP a good choice for an initial packing if we want to examine a system where weakening after faulting is important (just how important depends on μ_e and on how constrained the system is).

To get an idea for what these parameters correspond to in accretionary wedges, suppose we assume that any pore pressure in the material is directly proportional to the normal stress acting perpendicular to the contact,

$$p_f = \varepsilon \sigma_n. \tag{1}$$

This is commonly done in fault mechanics studies (Harris 1998). In this case, μ_e can be called the 'effective' coefficient of friction modified to include the effect of pore pressure (Harris 1998), i.e.

$$\mu_e = \mu_e^{dry}(1 - \varepsilon), \tag{2}$$

where μ_e^{dry} is the dry friction value. Low values of μ_e therefore correspond to either low values of μ_e^{dry} with low p_f or high values of μ_e^{dry} with high values of p_f. The pore pressure is assumed to be distributed in such a way as to maintain a constant μ_e. A similar argument is used for the element to wall friction, μ_b.

If we assume that the normal stress acting between the elements is lithostatic and the fluid pressure is hydrostatic, then ε in eq. (2) is the ratio of the density of water (1000 kg m^{-3}) to the density of the crust (in the range 2300–2800 kg m^{-3}) or about 0.35. From eq. (2), the effective friction is therefore about 0.5 (depending on the crustal density) if the dry value is 0.8 (Byerlee 1978). Hence, we will use $\mu_e = 0.5$ as our 'standard' value for μ_e. However, drilling results have indicated fluid pressures that are higher than the hydrostatic fluid pressure in a number of localities [e.g. Taiwan (Dahlen 1984)]. If these values are typical and remain high over geological timescales, then the effective friction coefficient to use could be lower than 0.5. On the other hand, it is also conceivable that the effective friction coefficient could be higher than 0.5. For example, this could occur if faults are 'smoother' at the laboratory scale than they are at the crustal scale. [A smooth surface is one where the standard deviation from the average height is orders of magnitude smaller than the scalelength of the surface. The smoothness of a surface will affect its average frictional strength and also its stick–slip behaviour (Fox *et al.* 1998)].

Material contrasts across the backstop or between the crust and the base may also lead to an effective coefficient of friction between the elements and the walls (μ_b) which is not the same as that between the elements (μ_e). Once again, μ_b could be higher or lower than 0.5.

The coefficients of friction (μ_e and μ_b) will therefore be considered as variables in this study. The primary aim of this paper will be to determine the effect of different values of μ_e and μ_b on the evolution of accretionary wedges and thrust belts.

2.5 Displaying the data

Three different types of diagrams will be used in the following sections. The first type of diagram will simply show the elements shaded according to their initial height. This allows the total amount of deformation to be seen. The second type shows the maximum displacement of any neighbour from a given element over approximately the last 100 000 steps (corresponding to about 1.8 km of convergence). In these diagrams, elements coloured in darker shades have experienced a large amount of displacement with respect to at least one of their neighbours. This allows faults to be more easily identified as dark lines against a grey background. This plot is analogous to an instantaneous strain rate plot in a continuum model (more accurately it is the 'recent' strain over the last few time steps). The neighbour of element i is defined to be any other element, j, the centroid of which is within a specified distance from the centroid of i. In DECM, this distance is 50 per cent greater than the sum of the radii of i and j. The third type of figure shows the total vertical displacement of each element over the same time interval in a reference frame stationary with respect to the base. Dark shades indicate a positive (upward) displacement of the element over that period. In some figures negative (downward) displacement may also be displaced as light shades of grey. These figures show the recent location of recent uplift and/or subsidence in the experiment.

Owing to space constraints, only some of the figures produced in this project will be displayed. More figures are posted on the web at http//:wwwrses.anu.edu.au/~davidb/cd2dmod.htm Interested readers can find links to more figures there.

3 RESULTS

3.1 Intermediate interelement friction $\mu_e = 0.5$

These runs correspond to crustal material that has a small pore fluid pressure, so that the element-to-element friction coefficient is slightly lower than the dry friction value of rocks (≈ 0.8, Byerlee 1978). The bulk friction value for one layer of elements could be different from this depending on the degree of interlocking. Fig. 4 shows the final step for a range of models with $\mu_e = 0.5$ and a variety of basal frictions, μ_b. As can be seen, there is a major difference between experiments with a weak base ($\mu_b \lesssim 0.4$) and those with a strong base ($\mu_b > 0.4$).

3.1.1 High to intermediate basal friction ($\mu_b > 0.4$)

Figs 5 and 6 show the evolution of a typical experiment with intermediate basal friction ($\mu_b = 0.5$). For these parameters, the experiment accommodates the deformation by oscillating between underthrusting and frontal accretion. The greater the basal friction the more time the experiment spends in the underthrusting mode. Note that the difference between the different panels in these figures is quite large (1.8 km of convergence). It can therefore appear that several faults are active at once (Fig. 5). Fig. 7 shows the deformation over a much smaller interval (91 m of convergence, or about 10 000 time steps) to show the amount of localization of deformation present in the experiment (this is closer to the instantaneous strain rate plot in a continuum model).

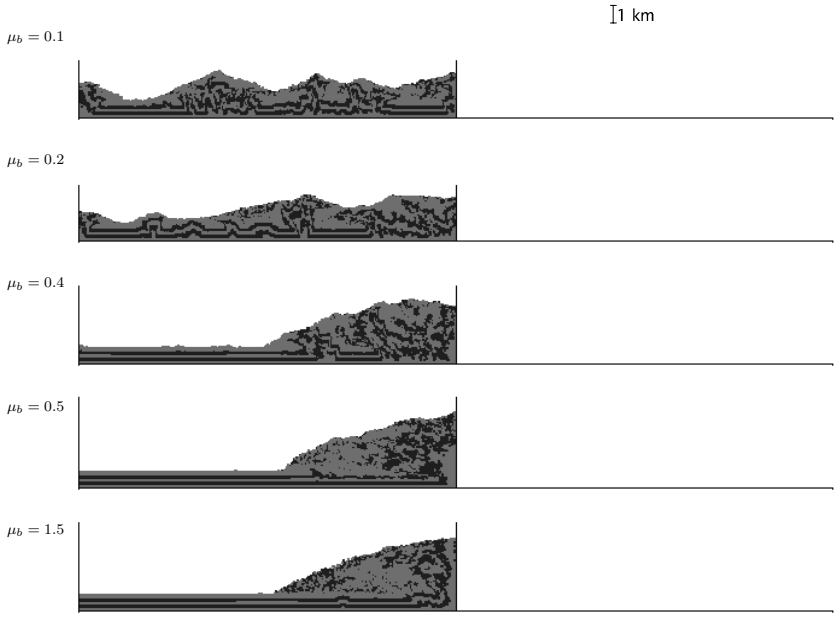

Figure 4. Final steps for experiments with $\mu_e = 0.5$ but different μ_b. The left-hand wall effects the low-μ_b experiments early in the run (which causes a pop-up structure to form near the left-hand wall). The length of the line to the right of the right-hand wall corresponds to the amount of compression completed to reach this point.

Underthrusting mode

During periods of underthrusting (e.g. stage *i* and *v* in Fig. 5), material is thrust beneath the toe of the wedge and uplifted near the rear of the wedge at a thrust fault close to the backstop. The thrust faults typically have a 'staircase' or ramp-flat structure. If the material is underthrust for a significantly long period, the slope of the prism can build up towards the angle of repose of the material and usually becomes increasingly linear. For very high basal friction values (above 0.8) the experiment is nearly always underthrusting (Fig. 4). As a result, the wedge grows roughly self-similarly with a constant slope (at the angle of repose). This can be seen in plots of the maximum height of any element in the wedge (see Fig. 8). For high μ_b values, the slope (α) is approximately constant, and therefore the width (w) of the wedge is a fixed fraction of the height h (i.e. $w = h/\tan\alpha$). If the area of the wedge increases approximately linearly with compression (i.e. $A \approx kt$), then this implies that $h \approx K\sqrt{(t)}$, where K is a constant. This is approximately the shape of the high-μ_b curve in Fig. 8.

Frontal accretion mode

Even for high μ_b values, the region of uplift occasionally jumps forward toward the toe as a pop-up structure and the system undergoes frontal (or near frontal) accretion (e.g. stage *ii* in Fig. 6). Pop-up structures usually form beyond the toe of the wedge or just underneath it. Initially, pop-up structures start symmetrically but evolve into the geometry of a strong pro-thrust and a number of weak retro-thrusts. The pop-up structure remains fixed in the reference frame of the accreting material. The separation between the right-hand wall and the pop-up structure therefore decreases (i.e the point of subduction and the pop-up structure approach each other). For the higher basal friction values, the model rapidly returns to the underthrusting mode and the pop-up structure becomes inactive.

For the intermediate-μ_b experiments the pop-up structure can remain active for several kilometres of convergence. Eventually, it reaches the backstop and the system returns to the underthrusting mode or possibly forms a new pop-up closer to the new toe of the wedge. The continued activity of the pop-up structure usually makes the overall slope of the wedge more parabolic. The steeper section of the wedge is always towards the toe of the pop-up structure and a more shallow slope develops to the right of the pop-up structure. Normal faulting can sometimes be seen near the top of the accretionary prism, particularly during the transition from underthrusting to these periods of frontal accretion modes (see Section 4.4). Some interlayer sliding between the initial layers of the pack can occasionally be seen (e.g. Fig. 6, panel *ii*). These usually terminate in smaller pop-up structures that do not extend to the base of the model. However, most of the horizontal deformation is along the base.

During periods of frontal accretion, the maximum height of any part of the experiment does not increase (see Fig. 8). In fact, the maximum height of the model often decreases just after the transition between the two modes caused by normal faulting and/or landsliding near the crest of the model.

3.1.2 *Low basal friction*

Figs 9 and 10, show part of a low basal friction experiment ($\mu_b = 0.2$). This type of experiment is closest to a typical analogue model that has a low-friction base (such as Mylar). However, it must be remembered that the model material is not isotropic owing to the initial packing.

Deformation with these parameters is dominated by frontal accretion and pop-up structures. The deformation often moves to the left-hand wall when the basal friction is very low. These experiments therefore more closely resemble the compression of a weak material between two strong regions ['vice' tectonics (Ellis *et al.* 1999)]. This is commonly observed in nature [e.g. the

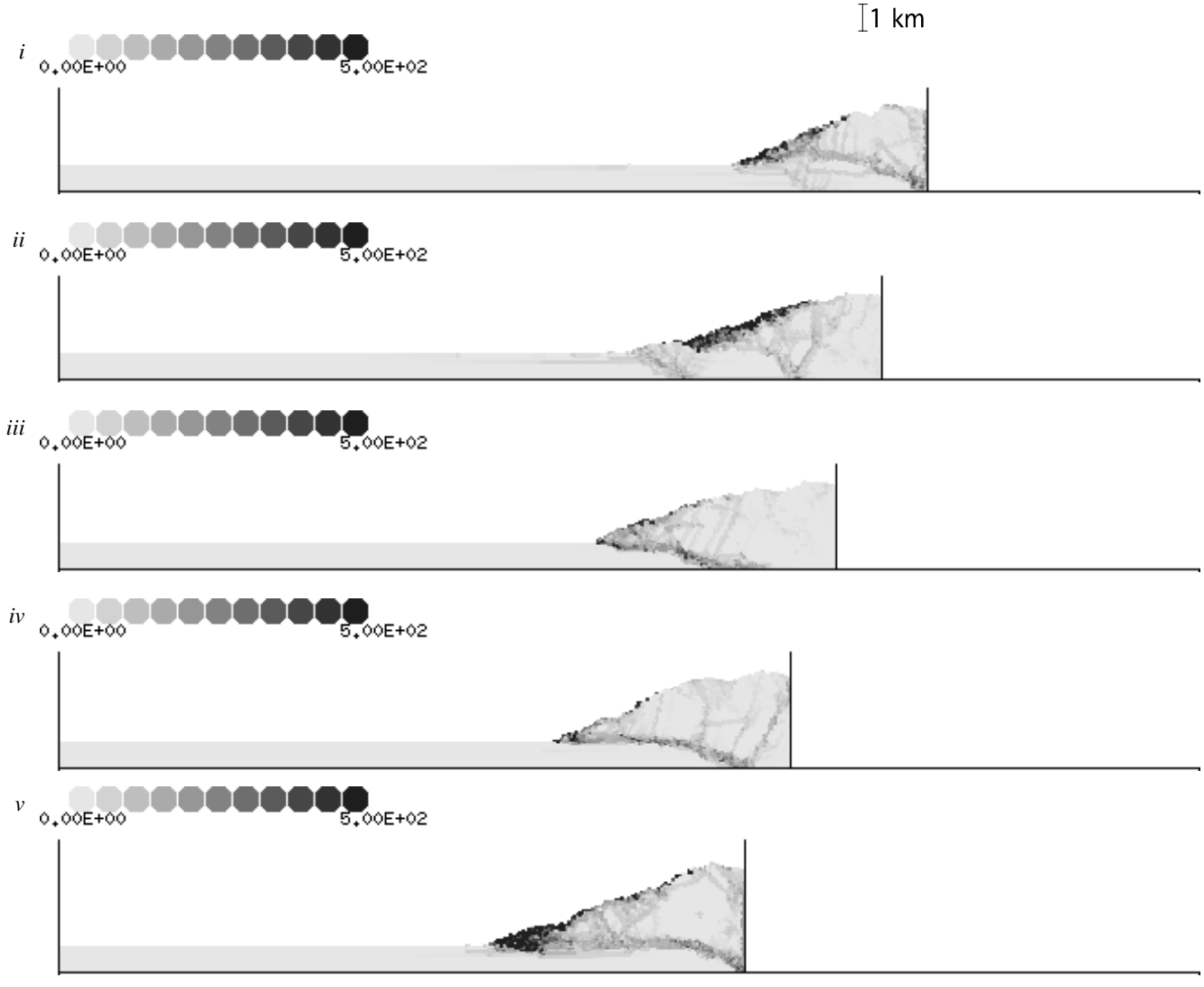

Figure 5. Part of the evolution of the model when $\mu_e = 0.5$ and $\mu_b = 0.5$, shaded to show the location of the recent displacement between neighbours. Elements are shaded according to the maximum change in separation between the elements and any of its neighbours from the current stage to the previous stage. So if a fault occurs between two elements they will both be shaded. The scale in this figure is in metres. Elements with a change in separation of greater than 500 m are shaded black. The few (highly compressed) elements with less than zero change in separation are all light grey. The interval between the stages corresponds to about 1.8 km of convergence. The model is underthrusting at stage i (10.9 km of compression), but a pop-up structure develops by stage ii (12.8 km of compression). At stage iii (14.6 km of compression), the pop-up structure is accommodating most of the deformation. Note that the pro-thrust is dominating the pop-up. By step iv (16.5 km of compression) the system is reverting back to underthrusting, and has completely reverted by stage v (18.3 km of compression). Note the change of overall slope and shape of the wedge during the oscillation.

Melbourne zone of the Lachlen Fold Belt (Cayley *et al.* 2000)]. If $\mu_b = 0$, the deformation quickly moves to the left-hand wall, no matter how far away it is. The higher μ_b, is the smaller the separation between the walls has to be before the left-hand wall affects the result.

There is never a smooth slope over the length of the model. Instead the surface is rough at the length-scale of the pop-up structures. At length-scales smaller than this, the slope can locally reach as high as the angle of repose of the material. The maximum height of these experiments therefore does not become as large as for the high basal friction models (Fig. 8).

The order of fault formation generally tends from right to left, although occasionally the location of the deformation can suddenly jump a substantial way into the model (several kilometres), only to return to the undeformed region later. This type of behaviour becomes more common at very low basal frictions (e.g. 0.1). If the basal friction is set to zero (e.g. lithostatic basal pore pressure), then the deformation oscillates between the left- and right-hand walls, until quite late in the deformation. Relatively little interlayer sliding occurs at these low values of basal friction.

After the initial separation between the walls has been reduced by 50 per cent, the final shape of the prism is dramatically different from the high basal friction experiments (Fig. 4). The boundary between experiments dominated by frontal accretion and those dominated by basal friction can clearly be seen in Fig. 11. In this figure we have plotted the average change in separation between the elements and their initial neighbours over all the elements in the model (which will be abbreviated to the average neighbour shift, or ANS). If no parts of the model

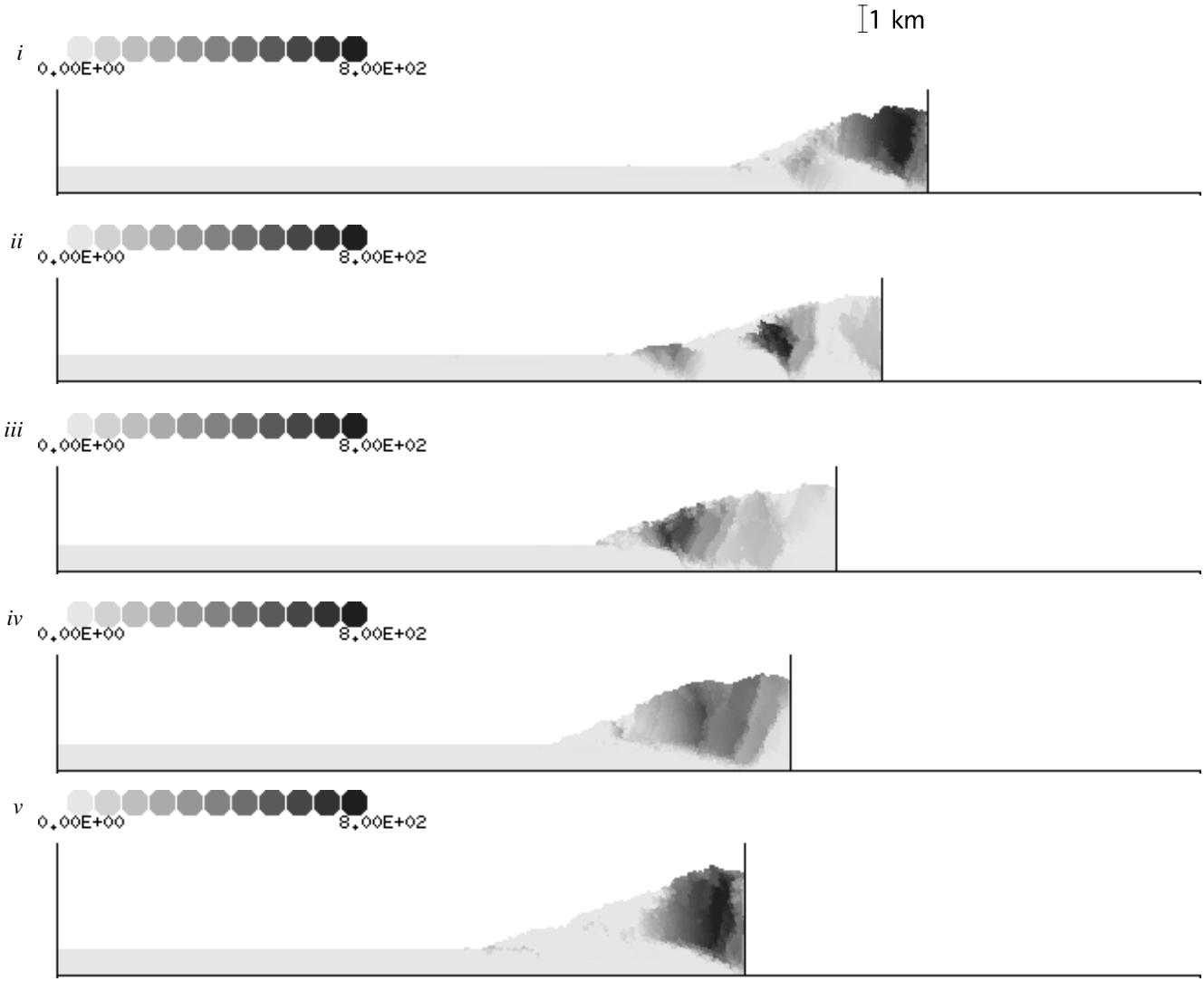

Figure 6. Part of a run with $\mu_e = 0.5$ and $\mu_b = 0.5$, shaded to show the positive (upward) vertical displacement over the period between the stages shown in Fig. 5. This shows the regions of uplift in the model between the stages shown in Fig. 5.

were deformed from its initial configuration, then there would be no change in separation. If there were a large amount of deformation from the initial configuration of elements, then this would cause a large change in the separation between them (in some cases a few kilometres) and hence give a large average neighbour shift. In essence, the average neighbour shift is a measure of how coherent the experiment remains after a given amount of deformation. The difference in ANS between the two modes increases with deformation as more elements are added to the prism (Fig. 11). For experiments dominated by back accretion, a large amount of deformation occurs within the prism. These experiments are therefore characterized by a large ANS. For experiments dominated by pop-up structures, the pop-up structures are smaller and often stop deforming when the location of the deformation moves to a new one. These experiments are therefore characterized by a smaller ANS than the back accretion experiments. In essence, the back-accretion-dominated experiments reduce the coherence of the experiment (in nature this would correspond to the production of a chaotic melange) more than the frontal-accretion-dominated experiments.

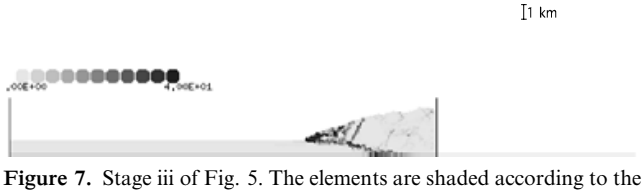

Figure 7. Stage iii of Fig. 5. The elements are shaded according to the amount of displacement over the last 91 m of convergence (as opposed to the last 1.8 km for Fig. 5).

3.2 High interelement friction, $\mu_e = 0.8$

These runs assume that the crustal material is extremely strong. This could be analogous to very dry pore pressure, so that the friction value is close to Byerlee's law (Byerlee 1978). The results for these runs are very similar to those observed with $\mu_e = 0.5$ (see Fig 12 for the final stage of the experiments for a range of μ_b). The main difference is the complete absence

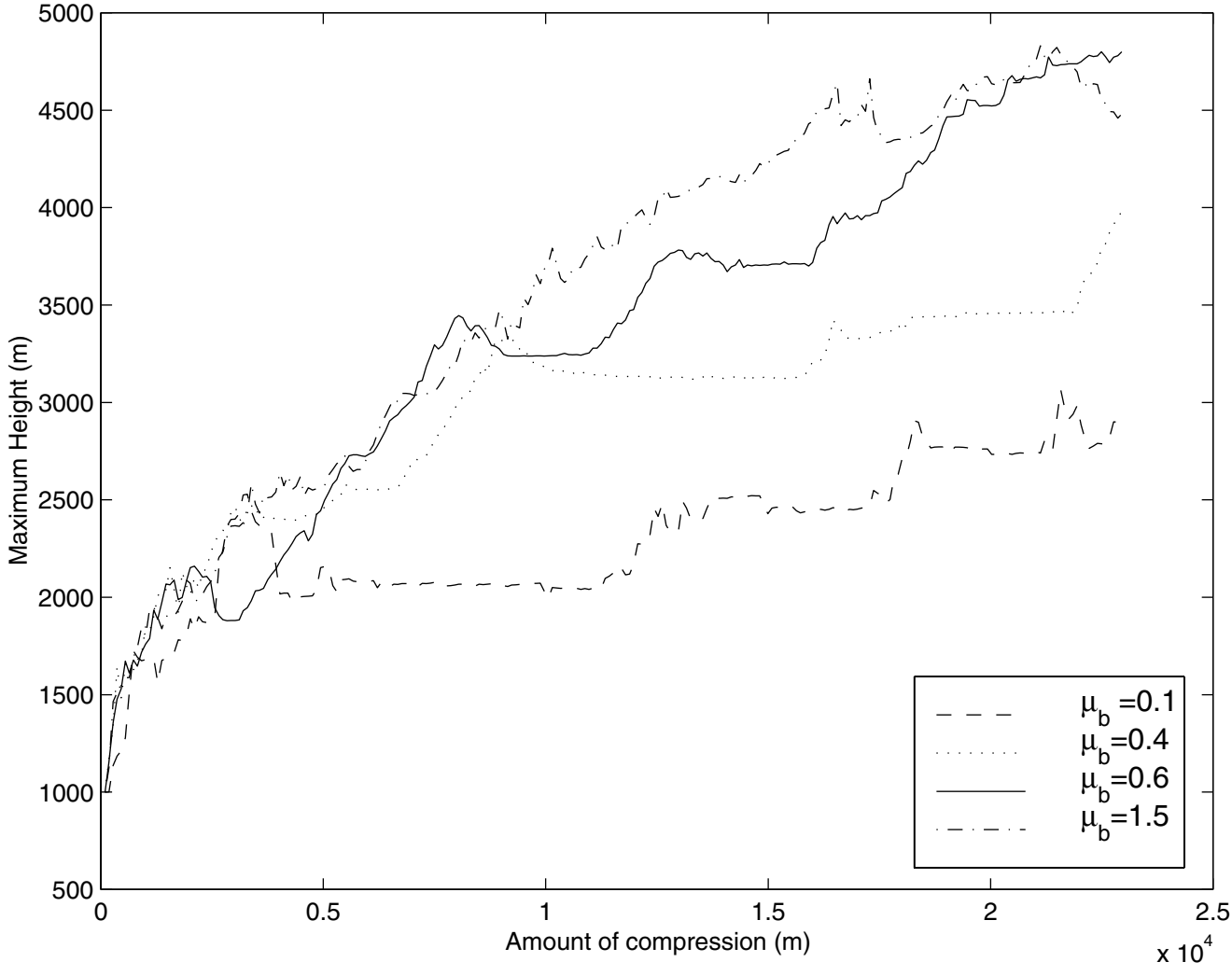

Figure 8. The change in the maximum height of any element in the model as a function of the amount of convergence for $\mu_e = 0.5$ and a variety of basal friction values.

of interlayer sliding at any point for most of the runs. The deformation usually concentrates along a few fault zones. The localization is thus very strong. Deformation at the left-hand wall also does not occur, or occurs after much more deformation, than for the lower μ_e runs with the same μ_b. The change in the ANS as a function of μ_b for the $\mu_e = 0.8$ experiments was similar to that for the $\mu_e = 0.5$ experiments (i.e. low ANS for $\mu_b < 0.4$ and high ANS when $\mu_b > 0.4$, see Fig. 11). The evolution of the maximum height in the $\mu_e = 0.8$ experiments was also similar to evolution of the maximum height in the $\mu_e = 0.5$ experiments (Fig. 8).

3.3 Low interelement friction, $\mu_e = 0.2$

These runs model the situation where the crustal material is weak, for example it may have a high pore pressure. Once again, frontal accretion dominates for low basal friction and back accretion dominates for high basal friction (see Fig. 13 for the final stage for a range of μ_b). One of the most striking differences is the large amount of interlayer sliding that occurs, particularly for the runs with a higher basal friction (see Fig. 14). The overall slope of these models is shallower than for the higher μ_e experiments. While the deformation is localized for short periods along faults, the location of the deformation tends to jump rapidly (i.e. within a few thousand steps) from one fault or sliding layer to another (Fig. 14). The final result is that the total deformation is considerably more distributed than for the higher interelement friction experiments (*cf.* Figs 12 and 13). Deformation at the left-hand wall also occurs earlier for these experiments, and is generally linked to the wedge at the right-hand wall by interlayer sliding (Fig. 14, bottom panel). The transition between the frontal-accretion-dominated experiments and the rear accretion experiments is less distinct for these low-strength experiments than it was for the experiments with a higher value of μ_e.

3.4 Comparison with observed geological structures

Many of the structures observed in these experiments are similar to structures observed in natural systems. As stated in

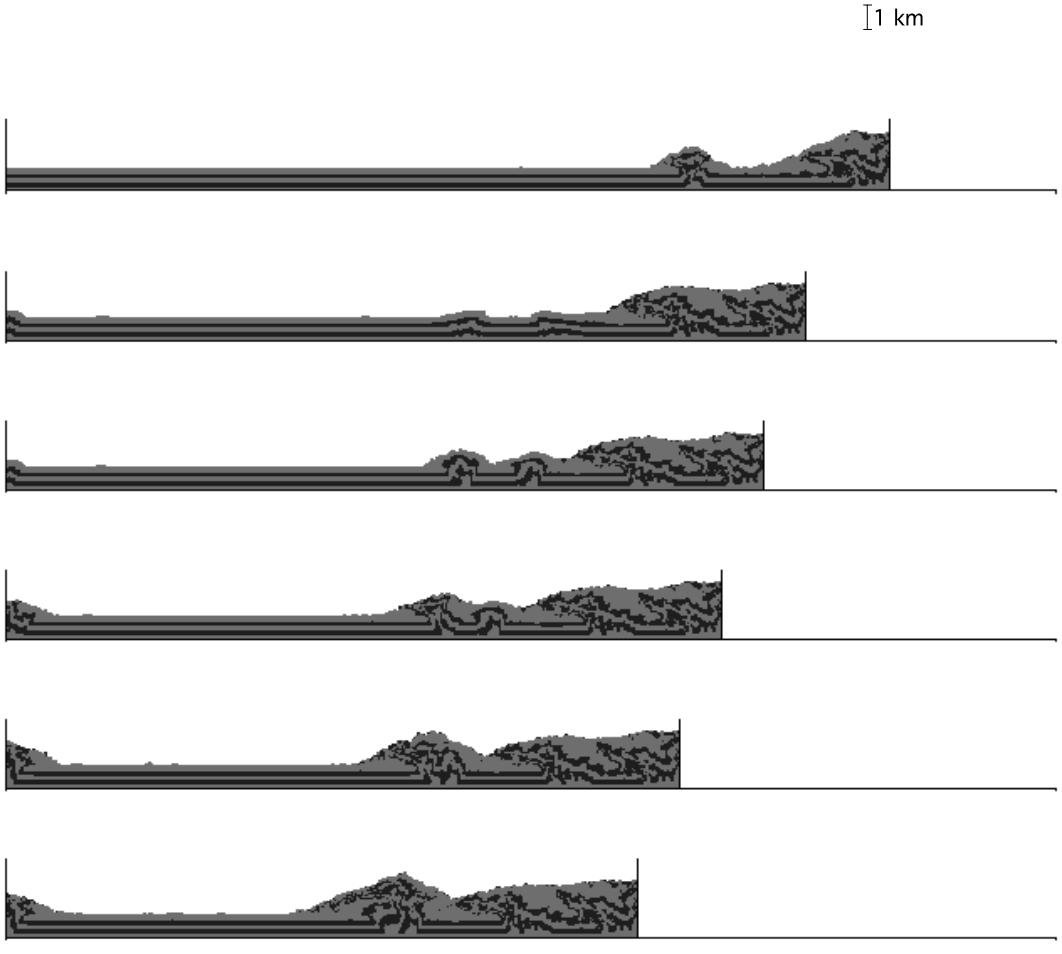

Figure 9. This shows part of a run with $\mu_e = 0.5$ and $\mu_b = 0.2$ (the weak base case). The elements are shaded according to their initial height. This run is dominated by pop-up structures and frontal accretion. Very little underthrusting occurs in these models. Deformation often moves to the left-hand wall quite early in these experiments.

the introduction, frontal accretion and back accretion are both observed as accretion mechanisms (Platt 1986). Fig. 15 shows three runs shaded into two layers. The experiments all have the same μ_e (0.5). This choice of shading shows the amount (if any) of exhumation of deeper material. As can be seen in Figs 15(b) and (c), back accretion results in the uplift of deeper material near the back of the wedge. As material is uplifted near the back, it is removed away from the top and rolls/slides to the toe of the wedge. Later landsliding then buries this material, leading to a complicated melange near the front of the wedge, and uplifted deeper rocks near the back of the prism. In contrast, the top layer of material is not removed from the top of the individual pop-up structures in the frontal accretion mode (see Fig. 15a). The only way for lower layers to be exhumed is if the top layers were removed by erosional processes other than mass slumping/landsliding (which are not included in the model).

One should also note that the predominant vergence of the faults in the strong base/underthrusting mode is pro-ward, while both pro- and retro-faults are equally common for the weak base case. This is very similar to the observed lack of dominant vergence observed in fold-and-thrust belts underlain by evaporites [which are likely to be weak (Davis & Engelder 1985)].

In all of the strong base experiments, the retro-thrust of pop-up structures usually does not accommodate much deformation after their formation. This is similar to some accretionary wedges, such as Nankai (Karig & Lundberg 1990). The pro-thrust usually dominates, and the system develops into the commonly observed 'staircase' fault structure (or flat-ramp–flat-thrust fault) observed in many layered systems (Park 1983).

The interlayer sliding that terminates in a small pop-up structure observed in the low-μ_e runs is also observed near the toe of some accretionary prisms (sometimes called the deformation front or protothrust zone). The decollement leading to it is often thought to be caused by high pore pressure (Moore 1989). In summary, the model reproduces a range of fault structures observed in a wide range of geological systems, thus demonstrating that the anisotropic, layered, 'granular' rheology used is a good model for the rheology of the crust.

Although it is not our intention to compare our results directly with sandbox experiments, the underthrusting mode observed by Gutscher *et al.* (1996) shows many similarities with our experiments. Although the details are different, the general pattern is quite similar, particularly with their $\mu_b = 0.5$ experiment. They also observed underthrusting under a ramp-flat structure oscillating with frontal accretion. Relatively strong retro-thrusts near the back of the prism during underthrusting

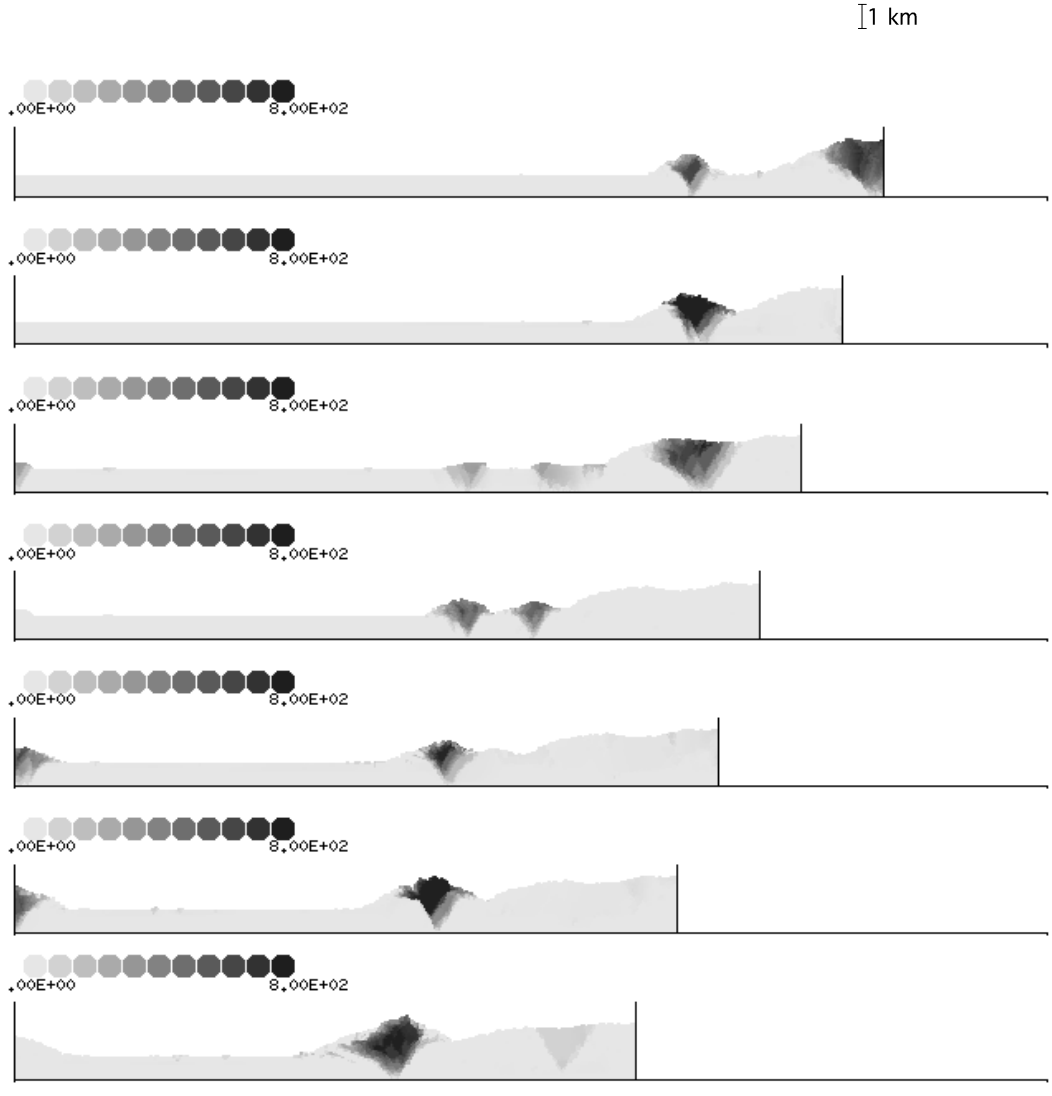

Figure 10. The same run as Fig. 9 ($\mu_e = 0.5$, $\mu_b = 0.2$). Elements are shaded according to their positive (upward) vertical displacement over the previous 1.8 km of convergence (i.e. between the stages shown in Fig. 9).

were also observed in both models. The only major difference is that in their model the frontal accretion mode is completely dominated by pro-thrusts, with no mention of any retro-thrusts (except for the initial two pro-thrusts). This is particularly apparent in their experiments with $\mu_b = 0.35$. This could be because of the dip of the base and/or the different initial conditions (our model has initial inhomogeneities for both types of thrust faults). This could be investigated in future work.

4 THEORY AND DISCUSSION

The observations described in the previous section can be explained with the use of work minimization theory, which falls into the category of variational principles stating that a system will evolve to maximize or minimize some particular quantity, in this case work. For simple problems, it can be proven that this method gives the same result as more classical methods (e.g force balance, Masek & Duncan 1998). However, this has not been done analytically for more complex, non-linear systems. Work minimization principles have been used to successfully provide a reasonably simple method for understanding some processes, including mountain building (Masek & Duncan 1998), the slip in duplexes (Mitra & Boyer 1986), and analogue models of strain partitioning in obliquely convergent boundaries (Burbidge & Braun 1998).

Strictly speaking, in order to use the work minimization theory we must prove that a given deformation mode requires less work than all other possible modes. To simplify the calculation, we will assume that there are just two possible modes of accommodating the deformation and assume that the model uses the one which requires the least amount of work. The two modes are:

(1) frontal accretion in a rectangular zone just beyond the pop-up structure; and

(2) uplift underneath the prism (either under the entire wedge or just the rear section of it).

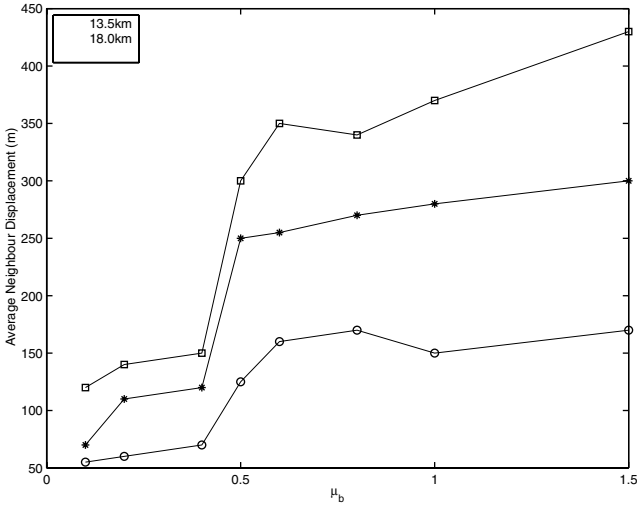

Figure 11. A plot of the average change in separation for all the elements in the model from their initial neighbours as a function of μ_b for a range of experiments with $\mu_e=0.5$. We call this change in separation the average neighbour shift. The ANS is analogous to the average total strain for all elements in a continuum model. The lines link experiments that all experience the same amount of compression. Experiments have a large ANS when the system is dominated by underthrusting (high μ_b). Models dominated by pop-up structures (low μ_b), have a significantly lower ANS.

This is a highly simplified view of the model but it illuminates the basic mechanics. The principle of this method is similar to that used by Gutscher *et al.* (1998a) to investigate the cyclicity of their sandbox experiments. The emphasis here is more on the required basal friction for the two different modes to dominate.

4.1 Frontal versus back accretion

4.1.1 Uplift under the entire wedge

Let h_0 be the initial height of the pack, let h_1 be the height of the uplifted triangular 'wedge' with slope α, let x_w be the width of the 'wedge' and let x_p be the width of a possible pop-up structure (Fig. 16). Assume that the material is incompressible. Let the right-hand wall compress the model by an amount dx. Assume that the model accommodates all of the deformation entirely by uplift under either the wedge (dy_w) or under a new pop-up structure (dy_p) by an infinitesimal amount. For uplift of the entire wedge, mass conservation imposes that

$$(h_1 + h_0)dx = x_w dy_w . \tag{3}$$

For uplift of the possible pop-up structure we have,

$$h_0 dx = x_p dy_p . \tag{4}$$

If uplift occurs at the pop-up structure, the wedge must slide along the base by an amount dx. Assume that the work required for any internal deformation (e.g. slip along any faults) is w_f^w for faults in the wedge and w_f^p for faults in the pop-up structure. The work required for back accretion, w_w, is therefore the change in potential energy plus w_f^w or,

$$w_w = \rho g x_w (h_1/2 + h_0) dy_w + w_f^w . \tag{5}$$

Substituting eq. (3) gives

$$w_w = \rho g (h_1/2 + h_0)(h_0 + h_1) dx + w_f^w . \tag{6}$$

For frontal accretion with a pop-up structure just beyond the toe, the total work required is the sum of the work required for

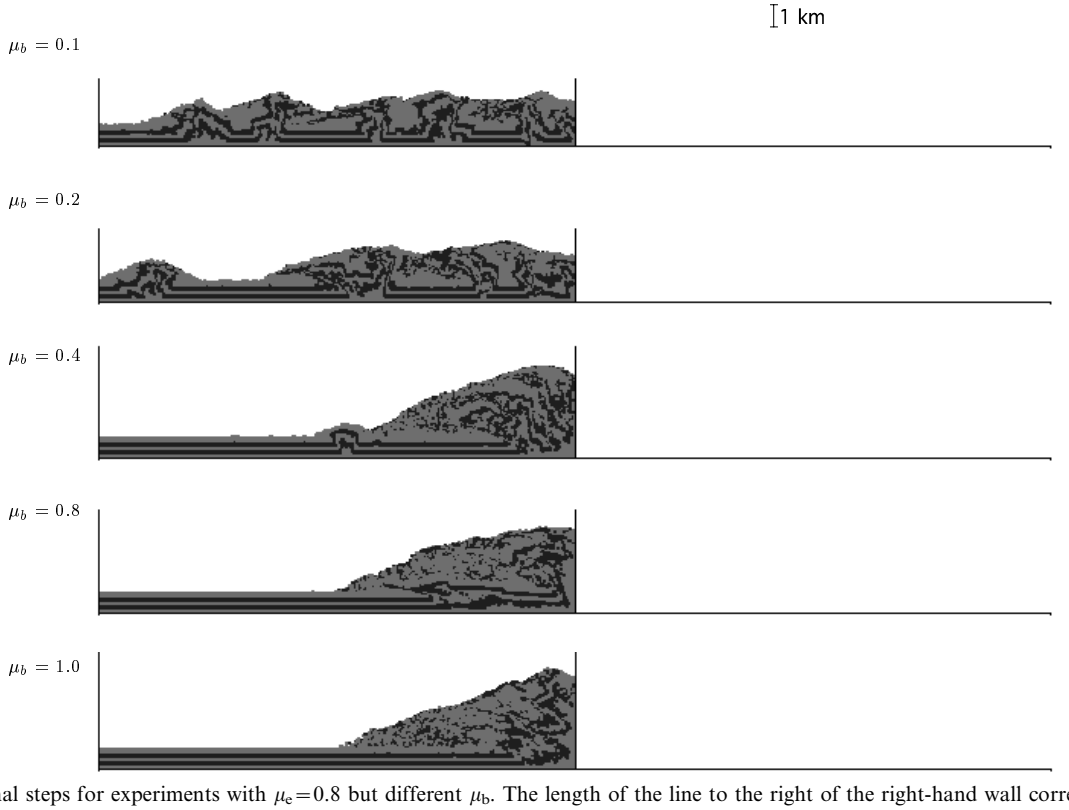

Figure 12. Final steps for experiments with $\mu_e=0.8$ but different μ_b. The length of the line to the right of the right-hand wall corresponds to the amount of compression completed to reach this point.

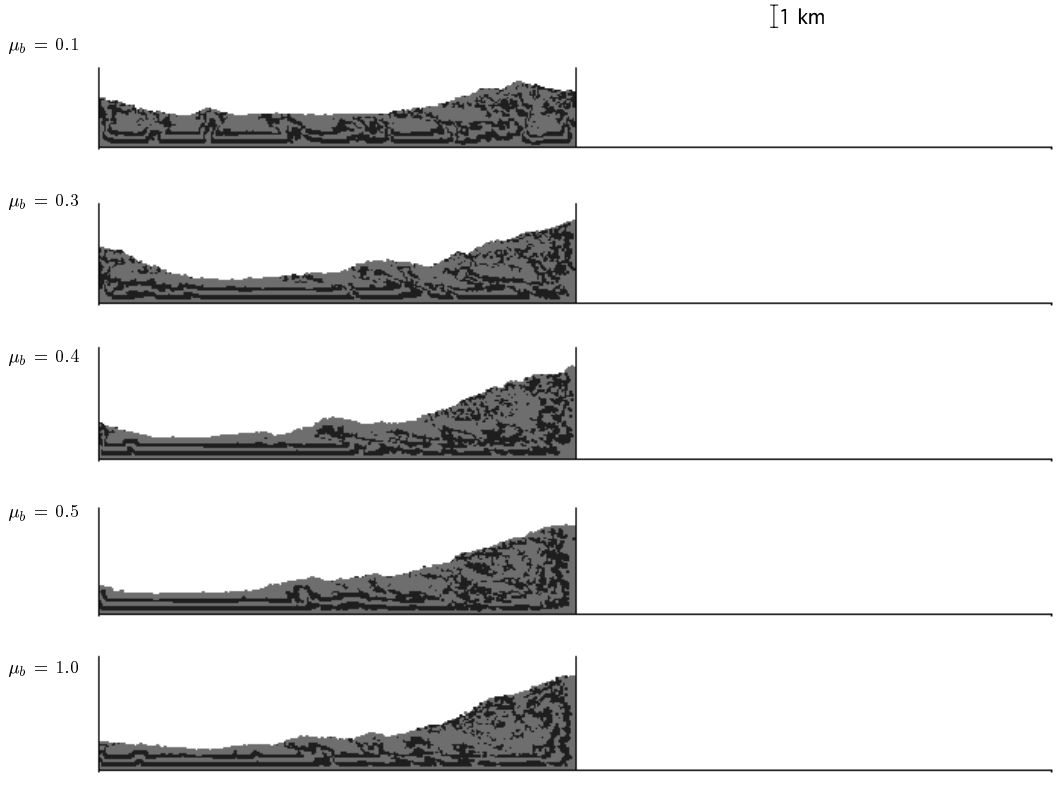

Figure 13. Final steps for experiments with $\mu_e = 0.2$ but different μ_b. The low-μ_b experiments are affected by the left-hand wall early in the run (which causes a pop-up structure to form near the left-hand wall). The length of the line to the right of the right-hand wall corresponds to the amount of compression completed to reach this point.

sliding the wedge, the work required for uplift and w_f^p,

$$w_p = \mu_b \rho g x_w (h_1/2 + h_0) dx + \rho g x_p h_0 dy_p + w_f^p . \quad (7)$$

Substituting eq. (4) gives,

$$w_p = \mu_b \rho g x_w (h_1/2 + h_0) dx + \rho g h_0^2 dx + w_f^p . \quad (8)$$

Let $\delta w_f = (w_f^w - w_f^p)/\rho g$. At the critical point when the work required for the two modes is equal we have,

$$\mu_b^{crit} x_w (h_0 + h_1/2) = (h_1/2 + h_0)(h_1 + h_0) - h_0^2 + \delta w_f \quad (9)$$

$$\mu_b^{crit} = \frac{h_1}{x_w} \frac{h_1 + 3h_0 + 2\delta w_f/h_1}{h_1 + 2h_0} . \quad (10)$$

From the diagram, $\tan\alpha = h_1/x_w$, so the critical value of μ_b is

$$\mu_b^{crit} = \tan\alpha \frac{h_1/h_0 + 3 + 2\delta w_f/(h_1 h_0)}{h_1/h_0 + 2} . \quad (11)$$

If the work required for internal deformation is approximately the same in both cases (i.e. there has been little weakening as a result of slip), then $\delta w_f \approx 0$. If we hold α constant we then have

$$\mu_b^{crit} = \tan\alpha \frac{h_1/h_0 + 3}{h_1/h_0 + 2} . \quad (12)$$

For very small values of h_1/h_0 then $\mu_b^{crit} \approx 1.5 \tan\alpha$. For very large values of h_1/h_0, $\mu_b^{crit} \approx \tan\alpha$. Therefore, μ_b^{crit} decreases as h_1/h_0 increases (i.e. as the wedge grows).

If μ_b is high enough (greater than 1.5 tan α) then the wedge may never enter the frontal accretion mode for any significant period of time, and so grow self-similarly at the angle of repose. For very low values of μ_b below tan α, the wedge may never enter the back accretion mode and deform by forming a series of pop-up structures in the frontal accretion mode.

In the experiments, α increases to a maximum of about 20° for $\mu_e = 0.5$ and 0.8. Hence μ_b^{crit} varies from about 0.36↔0.55. This is consistent with the transition between underthrusting and frontal accretion seen in the $\mu_e = 0.5$ and 0.8 experiments (Fig. 11). The transition for $\mu_e = 0.2$ is not as clear. This could be because of the large amount of interlayer sliding in this experiment. It is possible for the basal friction to be high, but the effective base could be higher up in the model between two layers. Since the interelement friction is low, the effective friction along this internal decollement would also be low. The typical slopes of these experiments are also lower, which would decrease μ_b^{crit} as well. Even so, there is still an observable transition between underthrusting-dominated experiments and frontal-accretion-dominated experiments (see Fig. 11).

4.1.2 *Partial uplift under the wedge*

As the wedge grows, the rear uplift zone does not encompass the whole of the wedge (see Fig. 16b). This makes the uplifting section of the wedge smaller. Let x_t be the length of the underthrust material (which does not uplift but does slide along the

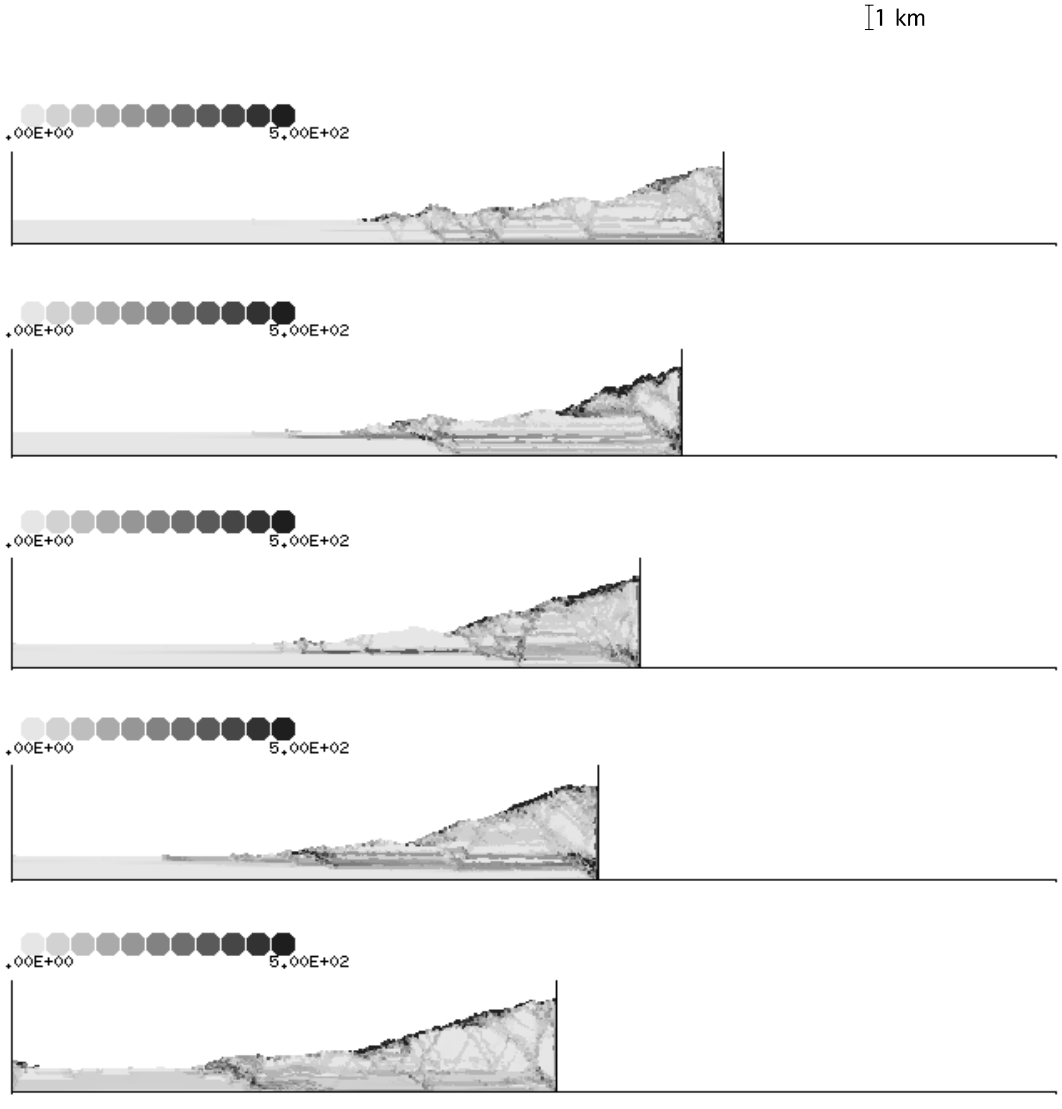

Figure 14. $\mu_e = 0.2$, $\mu_b = 0.5$. Elements are shaded according to the maximum neighbour shift between the elements over the previous 1.8 km of convergence. There is a large amount of interlayer sliding superimposed over the normal thrust fault structure. The interlayer sliding occurs along the initial horizontal layers in the crust.

base). The work required to uplift at the back of the wedge is,

$$w_w = \rho g \left[\frac{1}{2} h_1 (x_w + x_t) - \frac{1}{2} x_t^2 \tan\alpha + x_w h_0 \right] dy_w + w_f^w . \quad (13)$$

Substituting eq. (3) gives,

$$w_w = \rho g \left[\frac{1}{2} h_1 \left(1 + \frac{x_t}{x_w} \right) - \frac{x_t^2}{2x_w} \tan\alpha + h_0 \right] (h_0 + h_1) dx + w_f^w . \quad (14)$$

For uplift at the front of the wedge we have,

$$w_p = \mu_b \rho g \left[\frac{h_1}{2} (x_w + x_t) + h_0 (x_w + x_t) \right] dx + \rho g x_p h_0 dy_p + w_f^p . \quad (15)$$

Substituting eq. (4) gives,

$$w_p = \mu_b \rho g (x_w + x_t) \left(\frac{h_1}{2} + h_0 \right) dx + \rho g h_0^2 dx + w_f^p . \quad (16)$$

Equating these two equations and rearranging for μ_b^{crit} gives (assuming $\delta w \approx 0$),

$$\mu_b^{crit} = \left[h_1 \left(1 + \frac{x_t}{x_w} \right) - \frac{x_t^2}{x_w} \tan\alpha + 2h_0 \right] \times \frac{h_1 + h_0}{(h_1 + 2h_0)(x_t + x_w)} - \frac{2h_0^2}{(h_1 + 2h_0)(x_t + x_w)} . \quad (17)$$

From Fig. 16(b), $\tan\alpha = h_1/(x_w + x_t)$, so we have,

$$\mu_b^{crit} = \tan\alpha \left[\left\{ 1 + \frac{x_t}{x_w} \left(1 - \frac{x_t}{h_1} \tan\alpha \right) \right\} \frac{h_0 + h_1}{h_1 + 2h_0} + \frac{2h_0}{h_1 + 2h_0} \right] \quad (18)$$

$$\mu_b^{crit} = \tan\alpha \left[\left\{ 1 + \frac{x_t}{x_w} \left(1 - \frac{x_t/h_0}{h_1/h_0} \tan\alpha \right) \right\} \times \frac{h_1/h_0 + 1}{h_1/h_0 + 2} + \frac{2}{h_1/h_0 + 2} \right] . \quad (19)$$

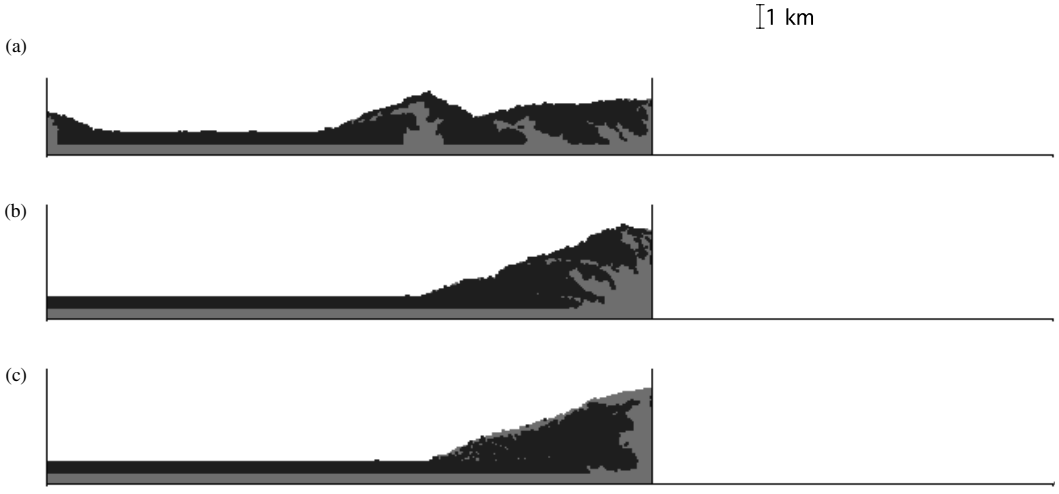

Figure 15. The same model as (a) Fig. 9 ($\mu_e=0.5$, $\mu_b=0.2$); (b) Fig. 5 ($\mu_e=0.5$, $\mu_b=0.5$) and (c) a model with a very high basal friction ($\mu_e=0.5$, $\mu_b=1.5$) with the elements initially shaded into two layers. The bottom half of the model is dark grey and the top half of the model is black. This shows the difference in the amount of exhumation of deep versus shallow rocks for the three different basal strengths.

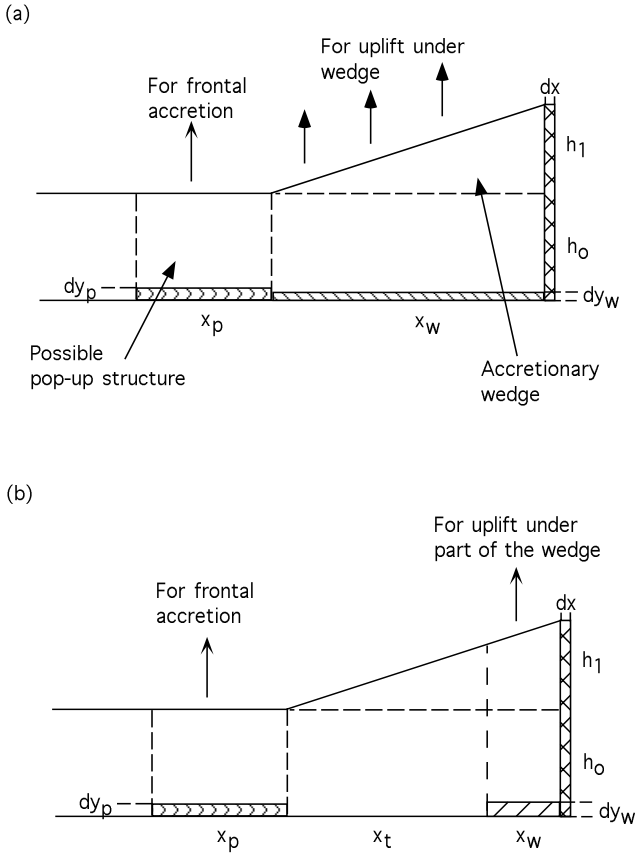

Figure 16. (a) Schematic diagram of the wedge where uplift occurs under the entire prism. x_p is the width of the possible pop-up structure, x_w is the width of the rectangular 'wedge', h_0 is the initial height of the material, h_1 is the height of the uplifted section, dx is the infinitesimal compression induced by the wall, dy_w is the infinitesimal uplift under the wedge and dy_p is the infinitesimal uplift under the pop-up structure. (b) Uplift now occurs under only part of the wedge (x_w). The part of the wedge that does not uplift has width, x_t.

If we hold α constant, then for large values of h_1/h_0, we have $\mu_b^{crit} \approx (1+x_t/x_w)\tan\alpha$. In the experiments, x_w is approximately constant and $x_t=h_1/\tan\alpha - x_w$. Hence μ_b^{crit} will become arbitrarily large so long as h_1 can increase. This means that for any value of $\mu_b > \tan\alpha$ the system will eventually require less work to form a pop-up structure for some value of h_1, i.e. the underthrusting mode must always swap to frontal accretion at some point, if h_1 is allowed to increase to a high enough value. In our experiments, some very small pop-up structures were observed to form even with basal friction as high as 1.5 (see the bottom panel of Fig. 4—note that in this figure the pop-up has been covered over by the prism but can still be seen in the underthrust segment). One experiment with $\mu_e=0.5$ and $\mu_b=100.0$ was also run, but no significant pop-up structures were observed. This indicates that for reasonable values of μ_b there should always be the occasional pop-up structure. If the material is very strongly attached to the base and not allowed to build up a high topography, then it might be possible to be in an effectively pure underthrusting mode, but this is likely to be rare in nature.

4.1.3 *Mode oscillation*

If μ_b^{crit} is smaller than the basal friction and the underthrusting is favourable, the wedge grows and α increases towards the angle of repose of the material. However, it is possible that μ_b^{crit} becomes higher than μ_b. At this point, the wedge may shift into the frontal accretion mode, and a pop-up structure should form. This causes the overall slope of the wedge to decrease and so shift the wedge back into the mode favouring back accretion. The wedge therefore oscillates between frontal and back accretion. Any pop-up structure that forms in the higher μ_b experiments, will tend to form closer to the backstop in order to minimize the total amount of basal sliding (and thus the work required). Even in our relatively simple numerical model, the real process is likely to be more complicated than the simple picture presented here. Factors such as the relative strengths of

intact and broken sections of the model will all have some influence on the evolution of the model. If the difference in strength is large then δw will not be approximately zero, and this will change when a shift in mode occurs (it will favour the currently active mode, since faulting weakens the crust). It is clear, however, that oscillation is still likely to occur, even in the simplest possible model and may thus be a common mode of deformation in real prisms.

4.2 Location of the deformation for the weak base case

For runs with very small values of $\mu_b \approx 0.2$, the location of the next pop-up structure may not necessarily be close to the front of the wedge (see Fig. 9). Instead, the location is often the left-hand wall, but it may also be a point within the model itself. Later in the run, the location of the uplift often jumps back between the pop-up structure and the front of the wedge (Fig. 9).

We believe that this behaviour arises from slight differences in the packing. If one element is only slightly displaced from another at some distance from the deformation front, then this may make this location slightly weaker than the area immediately to the left of the front. Since the left-hand wall is smooth and there is a velocity discontinuity there, it is clearly always a weak area compared with the interior of the pack. When the basal friction is very low, the difference in the amount of work required to break the pack in the two locations may be larger than the extra amount of work required to slip along the base between them. When basal friction is high, the work required for sliding across the base is more important, and (for the regular initial pack used in the model) it is likely to be more important than the difference in work required to break the initial packing at two different points within the model or the left-hand wall. Thus, the model attempts to minimize the amount of slip along the base and the deformation tends to move from right to left in a more 'orderly' fashion (i.e. without skipping potential pop-up structures).

In general, the deformation then tends to use a given pop-up structure exclusively until uplift of the pack within the pop-up structure adds so much work for further uplift that it becomes more favourable to break the initial packing in a new area. The 'critical' amount of uplift required for the deformation to jump to a new pop-up structure depends on the difference between the amount of weakening between the initial packing and the undeformed regions.

The effect of packing inhomogeneities is illustrated in Fig. 17, which shows results from an experiment in which inhomogeneities have been imposed *ab initio*. In this experiment the number of initial layers of the model changes from 20 at the right-hand wall to 10 at the left-hand wall in steps of 1. The points at which the number of layers change are indicated by arrows in Fig. 17. As can be seen, the formation of the pop-up structures always centres on the break in the packing (the inhomogeneity) and moves from right to left in a regular way. In summary, the exact location of the deformation depends on slight differences in the packing, and the height of pop-up structures (i.e. the amount of deformation accommodated) probably depends on the degree of weakening introduced by inhomogeneities.

For the real crust, this would mean that the location of the deformation will be much more sensitive to slight weakness in the crust, when the base is weak. The sequence of activity may not form an orderly progression across the deforming region but may jump unpredictably and chaotically from one area to another in response to very small changes in the initial strength of the material. Such weak zones could be caused by pre-existing faults, structural changes or changes in pore pressure. Effectively, the penalty for using zones of weakness further away is smaller when the basal friction is low and so remote weak regions are more likely to be activated.

4.3 Interlayer sliding

The observed reduction in the amount of interlayer sliding with increasing μ_e has a simple explanation when work minimization is used. Clearly, when the interelement friction is low, less work is required to slide along an internal surface than when the interelement friction is high. This is also related to the reason why long-term localization is less prevalent in the low-μ_e experiments. When μ_e is low, the difference between the strength of the intact sections of the pack and 'broken' sections along faults is much smaller than for the high-μ_e experiments. To demonstrate this, a very high interelement friction experiment was conducted ($\mu_e = 10.0$, see Fig. 18). No interlayer sliding is seen in these runs at all, and deformed sections of the experiment continue to be used even when they are strongly translated (see Fig. 18). This shows that for high values of μ_e, the benefit from breaking the initial packing (i.e. the reduction of work) is greater than for low values of μ_e and thus deformation localization is stronger. This reduction also means that δw_f is not even approximately zero when $\mu_e = 10.0$ (the current mode will always be favoured since the work required for internal deformation will be less there than it is in an unbroken section of the experiment).

4.4 Normal faulting

Small normal faults are occasionally seen near the surface of the model after long periods of underthrusting when the slope has reached the angle of repose of the system and elements are 'rolling' down to the toe of the model (e.g. Fig. 19a). However, these are transient features and do not last a significantly long time (more than a few thousand time steps). Large normal faults, which often propagate deep into the model (possibly as deep as the base of the model) are observed just after the transition from frontal accretion to rear accretion (see Fig. 19b).

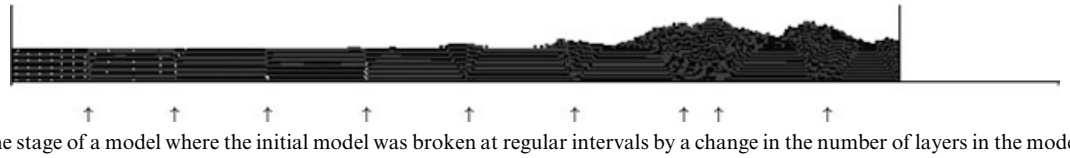

Figure 17. One stage of a model where the initial model was broken at regular intervals by a change in the number of layers in the model at the arrows ($\mu_e = 0.5$, $\mu_b = 0.2$). The arrows on the right-hand side of the model are closer together owing to the compression. The breaks in the packing produce an initial perturbation in the strength of the material at these points which causes the pop-up structure to form preferentially at these breaks.

Figure 18. Part of the evolution of a very high internal strength model with high wall friction ($\mu_e = 10.0$, $\mu_b = 0.8$). Elements are shaded according to maximum neighbour shift over the previous 1.8 km of convergence. The shear zone where the pack has been broken continues to be used even after it has been displaced from its optimal position. Localization is very strong.

These faults are similar to large normal faults often seen near the crest of accretionary prisms/thrust belts, e.g. Taiwan (Crespi *et al.* 1996). Numerous explanations of normal faulting have been offered (Willett 1999). In the case of our experiments, it seems that the transition to frontal accretion reduces the horizontal stress at the back of the model sufficiently to cause extension in this region, while compression and uplift still occur near the front of the model. This is in contrast with Willett's (1999) conclusions that, based on the results of finite-element models, normal faults are never observed in a doubly vergent wedge with a Coulomb rheology. However, Willett (1999) only considered the case of a weak base relative to the model material and he used slightly different rheology and boundary conditions (no rigid backstop). In our model, the model is discrete and considers high basal frictions. To the best of the authors knowledge, ours is the only numerical model that considers the very-strong-base case. Since this produces underthrusting (which is an observed mode of deformation in accretionary prisms) we suggest that future models (using the continuum approach, for example) should consider a wider range of basal strengths.

5 CONCLUSIONS

A new type of numerical model of crustal deformation based on the distinct-element method has been developed. It allows us to model deformation of the upper crust as that of a discontinuum, instead of as a continuum. The principle is similar to modelling the crust with an analoguous model that uses sand. Numerous runs were made over a wide range of frictional parameters. The resulting faulting structures show great similarities to those of various accretionary wedges and fold-and-thrust belts worldwide.

(1) For the weak base (low-friction) cases, pop-up structures forming beyond the toe of the wedge are the main structures present and the mode of accretion is entirely frontal. This situation is analogous to a fold-and-thrust belt sliding over evaporites (Davis & Engelder 1985). Low basal friction experiments are more sensitive to inhomogeneities in the initial packing, and the deformation may loosely be called more 'chaotic' (in the sense that small differences in the model can lead to large differences in the evolution).

(2) For the very strong base case, the deformation is mostly via the back accretion mode. Incoming material underthrusts the wedge and is uplifted near the back of the wedge using a 'staircase' (ramp-flat) thrust fault structure. The ramp remains fixed in the reference frame of the incoming material and is accreted into the wedge as the backstop moves towards it. Pro-thrusts are dominant in this mode, and any retro-thrust only accommodates a small amount of deformation and are often more numerous. Underthrusting usually dominates this mode, and deep material is often uplifted near the rear of the wedge.

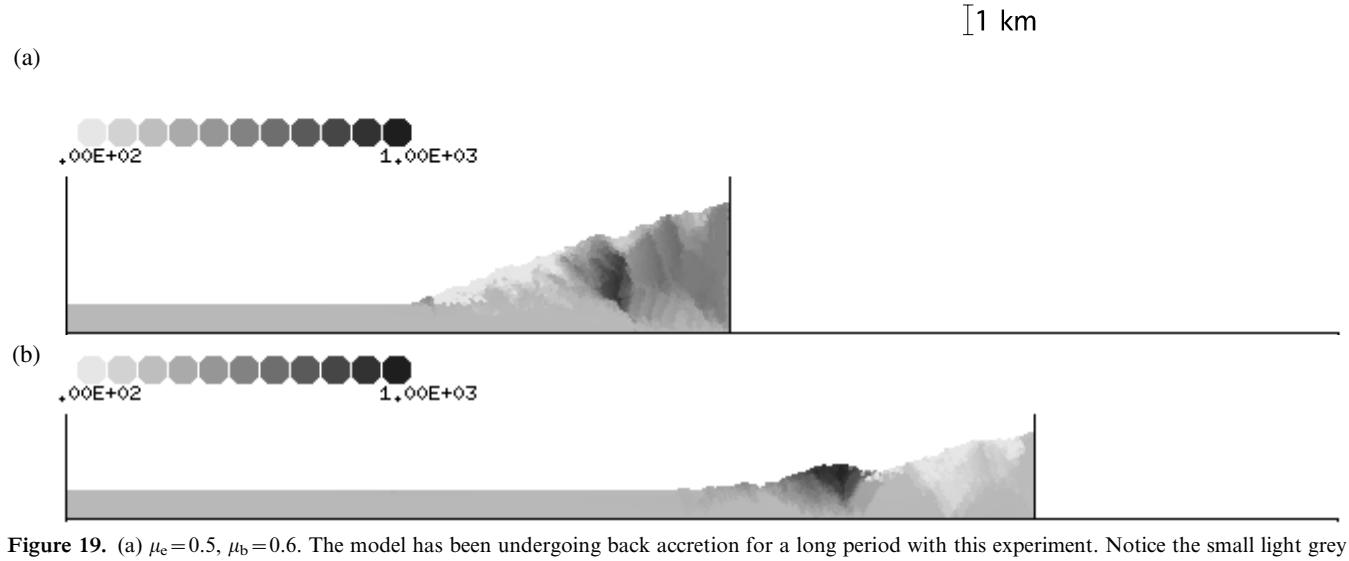

Figure 19. (a) $\mu_e = 0.5$, $\mu_b = 0.6$. The model has been undergoing back accretion for a long period with this experiment. Notice the small light grey triangular regions near the surface, which indicate that these regions are going down. These regions are bounded by small normal faults. (b) $\mu_e = 0.5$, $\mu_b = 0.4$. At this point the model changes from frontal to rear accretion. The conjugate faults near the back of the model indicate that material in this region is going down relative to the base (i.e. these faults are large normal faults).

(3) For intermediate values of basal friction, the wedge oscillates between frontal accretion and back accretion, with increasing lengths of time spent in the back accretion mode for higher values of basal friction. The results in these experiments may explain the variation in surface slope and faulting structure seen in some accretion wedges along their strike, as they may be in different phases of this oscillation (Gutscher *et al.* 1998a,b). To explain this behaviour, we propose a simple linearized theory based on the work minimization principle. To the best of the authors' knowledge, this is the first time a numerical model has reproduced this kind of behaviour. Our work, together with the analogue models of Gutscher *et al.* (1996, 1998a,b), imply that the steady-state model of the growth of an accretionary prism at a constant taper may not be correct, and the natural method of accretion in prisms is an oscillation between frontal and rear accretion.

(4) Large synorogenic normal faults are observed near the crest of the prism during the transition from frontal to rear accretion. After long periods of frontal accretion, the other, smaller normal faults are observed near the surface. These arise from a downslope extension to maintain the angle of repose of the material.

(5) Interelement sliding between the initial layers of the material is observed to become more prevalent in experiments where the internal (interelement) friction is smaller, and becomes a major factor for experiments with a very low value ($\mu_e = 0.2$). Conversely, localization along a few major faults becomes stronger as the interelement friction is increased.

REFERENCES

Allen, M.P. & Tildesley, D.J., 1987. *Computer Simulation of Liquids,* Clarendon Press, Oxford.

Beaumont, C., Fullsack, P. & Hamilton, J., 1994. Styles of crustal deformation in compressional orogens caused by subduction in the underlying lithosphere, *Tectonophysics,* **232,** 119–132.

Burbidge, D.R., 2000. The complex evolution of accretionary wedges and thrust belts: results from numerical experiments using the distinct element method, *PhD thesis,* Australian National University, Canberra, ACT, Australia.

Burbidge, D.R. & Braun, J., 1998. Analogue models of oblique convergent continental plate boundaries, *J. geophys. Res.,* **103,** 15 221–15 237.

Byerlee, J., 1978. Friction of rocks, *Pure appl. Geophys.,* **116,** 615–626.

Cayley, R., Taylor, D., Van der Berg, F. & Moore, D., 2000. The Western Lachlan Fold Belt, Southeast Australia doubly vergent fold belt formed by continental collision with an intervening weak zone, *Geological Society of Australia, Abstracts* No. 59.

Cobbold, P.R. & Castro, L., 1999. Fluid pressure and effective stress in sandbox models, *Tectonophysics,* **301,** 1–19.

Cowan, D.S. & Silling, R.M., 1978. A dynamic, scaled model of accretion at trenches and its implications for the tectonic evolution of subduction complexes, *J. geophys Res.,* **83,** 5389–5396.

Crespi, J.M., Chan, Y.-C. & Swaim, M.S., 1996. Synorogenic extension and exhumation of the Taiwan hinterland, *Geology,* **24,** 247–250.

Cundall, P.A. & Hart, R.D., 1989. Numerical modeling of discontinua, in *Proc. 1st US Conf. on Discrete Element Methods,* ed. G.G.W. Mustoe, M. Henriksen & H.-P. Huttelmaier.

Cundall, P.A. & Strack, O.D.L., 1979. A discrete numerical model for granular assemblies, *Géotechnique,* **29,** 47–65.

Dahlen, F.A., 1984. Noncohesive critical Coulomb wedges: an exact solution, *J. geophys. Res.,* **89,** 10 125–10 133.

Davis, D.M. & Engelder, T., 1985. The role of salt in fold-and-thrust belts, *Tectonophysics,* **119,** 67–88.

Davis, D., Suppe, J. & Dahlen, F.A., 1983. Mechanics of fold-and-thrust belts and accretionary wedges, *J. geophys Res.,* **88,** 1153–1172.

Ellis, S., Beaumont, C., Jamieson, R. and Quinlan, G., 1999. Continental collision including a weak zone: the vise model and its application to the Newfoundland Appalachians, *Can. J. Earth Sci.,* **35,** 1323–1346.

Fox, D.J., Kana, D.D. & Hsiung, S.M., 1998. Influence of interface roughness on dynamic shear behavior in jointed rock, *Int. J. Rock Mech. Min. Sci.,* **35,** 923–940.

Gulick, S.P.S., Meltzer, A.M. & Clarke, S.H., 1988. Seismic structure of the southern Cascadia subduction zone and accretionary prism north of the Mendocino triple junction, *J. geophys. Res.,* **103,** 27 207–27 222.

Gutscher, M-A., Kukowski, N., Malavieille, J. & Lallemand, S., 1996. Cyclical behavior of thrust wedges: insights from high basal friction sandbox experiments, *Geology,* **24,** 135–138.

Gutscher, M-A., Kukowski, N., Malavieille, J. & Lallemand, S., 1998a. Episodic imbricate thrusting and underthrusting: analog experiments and mechanical analysis applied to Alaskan Accretionary Wedge, *J. geophys Res.,* **103,** 10 161–10 176.

Gutscher, M.-A., Kukowski, N., Malavieille, J. & Lallemand, S., 1998b. Material transfer in accretionary wedges from analysis of a systematic series of analog experiments, *J. Struc. Geo.,* **20,** 407–416.

Harris, R.A. 1998. Introduction to special section: Stress triggers, stress shadows, and implications for seismic hazard, *J. geophys Res.,* **103,** 24 347–24 358.

Homberg, C., Hu, J.C., Angelier, J., Bergerat, F. & Lacombe, O., 1997. Characterization of stress perturbations near major fault zones: insights from 2-D distinct-element numerical modelling and field studies (Jura Mountains), *J. Struc. Geo.,* **19,** 703–718.

Hryciw, R.D., Raschke, S.A., Ghalib, A.M., Horner, D. & Peters, J.F., 1997. Video tracking for experimental validation of discrete element simulations of large discontinuous deformations, *Comp. Geotach.,* **31,** 235–253.

Hubbert, M.K., 1937. Theory of scale models as applied to the study of geological structures, *Geol. Soc. Am. Bull.,* **48,** 1459–1520.

Johnson, K.L., 1985. *Contact Mechanics,* Cambridge University Press, Cambridge.

Karig, D.E. & Lundberg, N., 1990. Deformation bands from the toe of the Nankai accretionary prism, *J. geophys Res.,* **95,** 9099–9109.

Kusky, T.M., Bradley, D.C., Haeussler, P.J. & Karl, S., 1997. Controls on accretion of flysch and mélange belts at convergent margins: Evidence from Chugach Bay thrust and Iceworm mélange, Chugach accretionary wedge, Alaska, *Tectonics,* **16,** 855–878.

Lallemand, S.E., Schürle, P. & Malavieille, J., 1994. Coulomb theory applied to accretionary and nonaccretionary wedges: possible causes for tectonic erosion and/or frontal accretion, *J. geophys Res.,* **99,** 12 033–12 055.

Lambe, T.W. & Whitman, R.V., 1968. *Soil Mechanics,* Wiley, New York.

Lui, H., McClay, K.R. & Powell, D., 1992. Physical models of thrust wedges, in *Thrust Tectonics,* pp. 71–81, ed. McClay, K.R., Chapman & Hall, London.

Masek, J.G. & Duncan, C.D., 1998. Minimum work mountain building, *J. geophys Res.,* **103,** 907–917.

Mitra, G. & Boyer, S.E., 1986. Energy balance and deformation mechanisms in duplexes, *J. Struc. Geo.,* **8,** 291–304.

Moore, J.C., 1989. Tectonics and hydrogeology of accretionary prisms: role of décollement zone, **11,** 95–106.

Mora, P. & Place, D., 1994. Simulation of frictional stick–slip instability, *Pure appl. Geophys.,* **143,** 61–87.

Morgan, J.K., 1999. Numerical Simulations of granular shear zones using the distinct element method 2. Effects of particle size distribution and interparticle friction on mechanical behaviour, *J. geophys Res.,* **104,** 2703–2719.

Oger, L., Savage, S.B., Corriveau, D. & Sayed, M., 1998. Yield and deformation of an assembly of disks subjected to a deviatoric stress loading, *Mechanics of Materials,* **27,** 189–210.

Pande, G.N., Beer, G., Williams, J.R., 1990. *Numerical Methods in Rock Mechanics,* Wiley, New York.
Park, R.G., 1983. *Foundations of Structural Geology,* Blackie, Glasgow.
Platt, J.P., 1986. Dynamics of orogenic wedges and the uplift of high-pressure metamorphic rocks, *Geol. Soc. Am. Bull.,* **97,** 1037–1053.
Saltzer, S.D. & Pollard, D., 1992. Distinct element modeling of structures formed in sedimentary overburden by extensional reactivation of basement normal faults, *Tectonics,* **11,** 165–174.
Sassi, W. & Faure, J.-L., 1987. Role of faults and layer interfaces on the spatial variation of stress regimes in basins: inferences from numerical modelling, *Tectonophysics,* **266,** 101–119.
Touloukian, Y.S., Judd, W.R. & Roy, R.F., 1989. *Cindas Data Series on Material Properties, II-2: Physical Properties of Rocks and Minerals,* ed. Touloukian, Y.S. & Ho, C.Y., Hemisphere, New York.
Turcotte, D.L. & Schubert, G., 1982. *Geodynamics: Applications of Continuum Physics to Geological Problems,* Wiley, New York.
Willett, S.D., 1999. Rheological dependence of extension in wedge models of convergent margins, *Tectonophysics,* **305,** 419–435.
Willett, S., Beaumont, C. & Fullsack, P., 1993. Mechanical model for the tectonic of doubly vergent compressional orogens, *Geology,* **21,** 371–374.

APPENDIX A: DETAILS OF THE NUMERICAL MODEL

A1 Finding the force

Suppose elements i and j are in contact and are separated by distance D_{ij}. A unit vector pointing from i to j is given by

$$\mathbf{e}^{ij} = \frac{\mathbf{x}^j - \mathbf{x}^i}{D^{ij}}, \tag{A1}$$

where $\mathbf{x}^i$ and $\mathbf{x}^j$ is the coordinate vector of the centroid of element i and j, respectively. Let $\mathbf{t}^{ij}$ be the unit vector at 90° to $\mathbf{e}_{ij}$ in the direction of positive shear displacement (defined to be anticlockwise). Let $\mathbf{y}^i$ and $\mathbf{y}^j$ be the shift in the centroid of elements from the previous time step for elements i and j, respectively. The relative displacement between the two elements is

$$\mathbf{\Delta X}^{ij} = \mathbf{y}^i - \mathbf{y}^j. \tag{A2}$$

The displacement normal to the contact X_n is the dot product of $\mathbf{\Delta X}^{ij}$ and $\mathbf{e}^{ij}$

$$X_n = \mathbf{\Delta X}^{ij} \cdot \mathbf{e}^{ij}. \tag{A3}$$

The displacement perpendicular to the contact (the shear displacement) is

$$X_s = \mathbf{\Delta X}^{ij} \cdot \mathbf{t}^{ij} - R(\delta\theta^i - \delta\theta^j), \tag{A4}$$

where $\delta\theta^i$ and $\delta\theta^j$ are the angular rotations over the previous time step and R is the radius (repeated indices do not imply summation). The increments to the normal and shear forces between the elements are defined to be

$$\Delta F_n = k_n X_n \tag{A5}$$

$$\Delta F_s = k_s X_s, \tag{A6}$$

where k_n and k_s are the elastic stiffnesses in the normal and shear directions to the contact, respectively. The stiffness can be allowed to vary from one element to another and could be modified at this point to incorporate more complicated stiffness models.

The increments of force are then added to the total normal and shear forces calculated from previous time steps for this particular contact, F_n and F_s. If $F_n < 0$ then all the forces from the contact are set to zero, i.e. there are no attractive forces between the elements. The total shear force, F_s, is also limited so that it is less than or equal to the shear force allowed by Coulomb friction given by

$$F_{max} = \mu F_n + c, \tag{A7}$$

where μ is the interelement friction coefficient (either μ_e or μ_b) and c is the interelement cohesion. In the current experiments c is set to zero. More sophisticated models of friction could potentially be incorporated at this step. For example, the friction could be reduced after a given amount of slip to include the effect of weakening. A more 'brittle' behaviour could be simulated by initially giving the elements a non-zero cohesion, which is then reduced to zero after a given amount of relative motion (e.g. Mora & Place 1994).

If contact damping is used, then a damping term (directly proportional to the relative velocity between the elements) is added to F_n and F_s. The time step in DECM can either be fixed or change through the experiment (dynamic time stepping) according to some pre-imposed criteria [e.g. Fehlberg dynamic time stepping (Stoer & Bulirsch 1993)]. Similarly, the damping can be fixed or dynamic. For the models described in this paper, the dynamic option was only used to find a first approximation to the correct values for a few test experiments (these involved allowing the elements to come to equlibrium and/or compressing the system slightly). The time step/damping was then fixed at a value slightly below this for all the future experiments. It is important to obtain the integration parameters correctly, since changing the damping from its 'optimal' value by (say) 50 per cent can change the amount of real time required for the system to come to equlibrium by an order of magnitude (Burbidge 2000).

The normal and shear forces exerted on the contact neighbour by element i are found using Newton's third law. The normal and shear forces are then resolved into components parallel to the x and y axes and added to the total force vector for all contacts on that element, F. The moment M is increased by the product of the radius times F_s.

The force exerted on an element by a contact with the wall is found in an analogous way. It is modelled as if the wall were a contact neighbour moving at the speed of the wall. The wall friction, stiffness and cohesion can be set to different values from the interelement values if desired.

A2 Updating the coordinates

Once the total force is found from all the contacts and from gravity, the force is used to find the translational and rotational acceleration using Newton's second law. The translational (separately in the x and y directions) and rotational velocity are updated using Euler's method,

$$v_x^{new} = v_x^{old} + a_x \delta t \tag{A8}$$

$$v_y^{new} = v_y^{old} + a_y \delta t \tag{A9}$$

$$v^{new} = v^{old} + \omega \delta t, \tag{A10}$$

where δt is the time step. The element coordinates are updated by integrating the velocity using the trapezoid method in order to provide better stability and accuracy than Euler's rule (Allen & Tildesley 1987).

$$x^{\text{new}} = x^{\text{old}} + (v_x^{\text{new}} + v_x^{\text{old}}) \frac{\delta t}{2} \tag{A11}$$

$$y^{\text{new}} = y^{\text{old}} + (v_y^{\text{new}} + v_y^{\text{old}}) \frac{\delta t}{2} \tag{A12}$$

$$\theta^{\text{new}} = \theta^{\text{old}} + (v^{\text{new}} + v^{\text{old}}) \frac{\delta t}{2} \tag{A13}$$

Higher-order methods were not used since they would require re-evaluating the forces several times for each step. This would greatly increase the length of computation time without a commensurate improvement in accuracy (Allen & Tildesley 1987).

A3 Updating the neighbours

In any DEM involving a large number of elements, it is crucial to find an efficient way of determining which elements are in contact. Simply checking whether any element is in contact with any other one by checking every other element in the model requires $n(n-1)/2$ calculations, where n is the number of elements (see Pande *et al.* 1990). This clearly becomes impractical for large values of n. Most methods reduce the number of calculations by only checking elements which are close to element i, these elements are called neighbours. At any time, only a subset of these neighbours is in contact with element i; these are termed contact neighbours. A good search scheme will check a minimum number of neighbours while ensuring that all the contact neighbours are found. The best way to do this depends on the exact nature of the problem. The current version of DECM uses a 'body-centred search scheme' (Pande *et al.* 1990). The contact information is stored in a neighbour list similar to those used in molecular dynamics models.